MNRAS 000, 1–19 (2023) Preprint 26 February 2024 Compiled using MNRAS LATEX style file v3.0

Radial halo substructure in harmony with the Galactic bar

Adam M. Dillamore,[1]★ Vasily Belokurov,[1] and N. Wyn Evans[1]
[1]Institute of Astronomy, University of Cambridge, Madingley Road, Cambridge CB3 0HA, UK

Accepted XXX. Received YYY; in original form ZZZ

ABSTRACT

Overdensities in the radial phase space (r, v_r) of the Milky Way's halo have previously been associated with the phase-mixed debris of a highly radial merger event, such as *Gaia* Sausage-Enceladus. We present and test an alternative theory in which the overdense 'chevrons' are instead composed of stars trapped in resonances with the Galactic bar. We develop an analytic model of resonant orbits in the isochrone potential, and complement this with a test particle simulation of a stellar halo in a realistic barred Milky Way potential. These models are used to predict the appearance of action space (J_ϕ, J_r) and radial phase space in the Solar neighbourhood. They are able to reproduce almost all salient features of the observed chevrons. In particular, both the analytic model and simulation predict that the chevrons are more prominent at $v_r < 0$ when viewed near the Sun, as is observed by *Gaia*. This is inconsistent with formation by an ancient merger event. We also associate individual chevrons with specific resonances. At a bar pattern speed of $\Omega_b = 35\ \mathrm{km\,s^{-1}kpc^{-1}}$, the two most prominent prograde chevrons align very closely with the corotation and outer Lindblad resonances. The former can be viewed as a highly eccentric extension of the Hercules stream. Finally, our model predicts that the v_r asymmetry changes sign as a function of Galactic radius and azimuth, and we find evidence that this is indeed the case in the Milky Way.

Key words: Galaxy: kinematics and dynamics – Galaxy: halo – Galaxy: structure

1 INTRODUCTION

In the days of the old quantum theory, Max Born developed perturbation theory to cope with the effects of resonances. This is summarized in his 1926 book *'The Mechanics of the Atom'*. When there are commensurable frequencies in a dynamical problem, Born showed how to perform a canonical transformation to a new set of action-angle coordinates – the so-called fast and slow action-angles. The basic idea is then to average over the rapid variations in the fast coordinates, keeping the slow variables fixed. Hamilton's equations then show that the fast action is constant or adiabatically invariant. This powerful technique was introduced into galactic dynamics by Lynden-Bell (1973) and exploited in the struggle to understand the origin of spiral structure and bar formation (e.g., Lynden-Bell 1979; Contopoulos 1979; Earn & Lynden-Bell 1996; Collett et al. 1997). It has also been widely used to model the capture of planets and planetesimals in solar system dynamics (e.g., Yoder 1979; Henrard 1982; Borderies & Goldreich 1984).

The influence of the Galactic bar on stars in the stellar disc has been long realised as substantial. Kalnajs (1991) made the pioneering suggestion that, if the Sun were located near a resonance, then there may be two stellar streams, one moving inward and the other outward. Resonant capture is an important mechanism for generating substructure in the stellar disc (e.g., Debattista & Sellwood 2000; Sellwood 2010; Gerhard 2011; McMillan 2013; Binney 2020; Chiba et al. 2021; Chiba & Schönrich 2021). With the advent of *Gaia* data, the ridges and features in the phase space distribution of disc stars have been subjected to scrutiny and often attributed to bar or spiral arm resonances (e.g., Fragkoudi et al. 2019; Khoperskov et al. 2020; Trick et al. 2021; Trick 2022; Khoperskov & Gerhard 2022; Wheeler et al. 2022).

By contrast, the effect of bar resonances in the halo has not received as much attention. Debattista & Sellwood (1998, 2000) demonstrated that dynamical friction from dark matter haloes acts to spin down bars. The phenomenon of dynamical friction is driven by the trapping of dark matter particles by the bar. This showed that resonances due to bars affect the dynamics of stars and dark matter in the halo, though the emphasis of the work was on implications for bar evolution and dark matter density. This has been further explored by Athanassoula (2002); Weinberg & Katz (2002); Ceverino & Klypin (2007); Collier et al. (2019); Chiba & Schönrich (2022); and Hamilton et al. (2023). The possibility of bar resonances creating substructures in the stellar halo was first suggested by Moreno et al. (2015, 2021). They showed that the trapping can extend several kpc above or below the Galactic plane and suggested that it may be the origin of some known moving groups. The first demonstration that this effect is present in the data on stellar halo stars was provided in Myeong et al. (2018) who noted the presence of a possible resonance in halo stars at all metallicities.

The *Gaia* Data Release 3 (DR3; Gaia Collaboration et al. 2023) provided a large sample of halo stars with full phase space coordinates around the Sun. Belokurov et al. (2023) exploited this to identify prominent chevrons in the space of radial position and velocity (r, v_r). These are the tell-tale signatures of shells, which are known to form in nearly radial mergers (e.g., Fillmore & Goldreich 1984; Quinn 1984; Amorisco 2017; Dong-Páez et al. 2022; Davies et al. 2023b). A natural conclusion was that the chevrons were caused

★ E-mail: amd206@cam.ac.uk (AMD)

by shells, expected from the last significant merger of the Milky Way with *Gaia* Sausage-Enceladus (GSE; Belokurov et al. 2018; Helmi et al. 2018).

Though natural, this conclusion does not appear to be correct. First doubts emerged with the realisation that the chevrons are present in comparatively metal-rich stars, whereas the dwarf progenitor is expected to be metal-poor. Only a very small fraction of the GSE stars have [Fe/H] > -0.7 (Naidu et al. 2020; Feuillet et al. 2021). The chevrons are also highly asymmetric in v_r, being only clearly visible at $v_r < 0$. Donlon et al. (2023) showed that this is inconsistent with the chevrons being dynamically old, and it is therefore difficult to explain how they could have been formed by the ancient GSE. They argued that this provides evidence of a more recent radial merger event in the last few Gyr, dubbed the Virgo Radial Merger (VRM).

However, the chevrons may not have been created by any merger event. Dillamore et al. (2023) demonstrated that similar structures are generated in simulations by the trapping of particles in resonances with the bar, with the corotation resonance being particularly prominent. Using a bar pattern speed in the range $\Omega_\mathrm{b} \approx 35 - 40$ km s^{-1} kpc^{-1} provides a good match both to the substructures in phase space and the measured speed of the Galactic bar (Sanders et al. 2019; Binney 2020; Chiba & Schönrich 2021). Davies et al. (2023a) also showed that non-resonant merger-generated chevrons may be destroyed by the rotating bar, raising doubts about their survivability in the Milky Way.

The purpose of this paper is to test the hypothesis that the chevron stars are trapped in bar resonances. In Section 2, we develop an analytic model of resonances in the isochrone potential. We then describe and present the results of our test particle simulation in Section 3 and *Gaia* data in Section 4. We analyse and compare the analytic model, simulation and data in Section 5 and present our conclusions in Section 6. Finally, Appendices A, B and C describe aspects of the analytic model and simulation in more detail.

2 ANALYTIC MODEL

In this section, we provide an analytic model of resonances with the bar. We treat the overall potential as the sum of a static spherical background potential Φ_0 and a small time-dependent non-axisymmetric perturbation Φ_b due to the bar:

$$\Phi(r, \theta, \phi, t) = \Phi_0(r) + \Phi_\mathrm{b}(r, \theta, \phi, t), \tag{1}$$

where (r, θ, ϕ) are Galactocentric spherical coordinates. In the unperturbed potential Φ_0, we may describe the orbits in terms of angle-action variables $(\boldsymbol{\theta}, \boldsymbol{J})$. The actions $\boldsymbol{J}$ are integrals of motion, so the unperturbed Hamiltonian can be expressed as a function of the actions only, $H_0(\boldsymbol{J})$. Hamilton's equations then read

$$\dot{J}_i = -\frac{\partial H}{\partial \theta_i} = 0 \tag{2}$$

$$\dot{\theta} = \frac{\partial H}{\partial J_i} \equiv \Omega_i(\boldsymbol{J}). \tag{3}$$

The angles $\boldsymbol{\theta}$ therefore evolve linearly in time. They are scaled such that one period corresponds to θ_i increasing by 2π, so that Ω_i are the fundamental frequencies of motion (Binney & Tremaine 2008). In the perturbed potential Φ, the actions $\boldsymbol{J}$ are no longer exact integrals of motion and the true frequencies are not equal to Ω_i. However, in the limit $|\Phi_\mathrm{b}/\Phi_0| \to 0$ the true frequencies tend to Ω_i (Trick et al. 2021). We use this weak bar limit in our model, so that Ω_i are good approximations to the true frequencies.

We consider resonances of the form

$$m(\Omega_\phi - \Omega_\mathrm{b}) + l\,\Omega_r = 0, \tag{4}$$

where Ω_ϕ and Ω_r are the azimuthal frequency and the radial frequency of oscillation respectively, and l and m are integers. We take the bar's pattern speed to be positive, $\Omega_\mathrm{b} > 0$. We emphasise that we use this equation to define both prograde and retrograde resonant orbits (i.e. both positive and negative Ω_ϕ)[1]. Studies of resonances in the disc frequently employ the epicyclic approximation (Binney & Tremaine 2008) to calculate Ω_ϕ and Ω_r for a perturbed circular orbit in a given potential. However, we wish to consider highly eccentric orbits, far from where this approximation is valid. In order to develop an analytic model of the resonances, we therefore wish to work in a potential in which equation 3 can be evaluated for all $\boldsymbol{J}$. Evans et al. (1990) showed that the most general potential for which the actions can be written in terms of elementary functions is the isochrone potential,

$$\Phi_\mathrm{I}(r) = -\frac{GM}{b + \sqrt{b^2 + r^2}}, \tag{5}$$

where M is the total mass and b is a scale length parameter. In the limit $r \to 0$ the potential tends to the harmonic limit of a homogeneous sphere, and when $r \to \infty$ it tends to the Keplerian limit of a point mass M. While Φ_I is too simple for modelling data in the Milky Way (for example, it is spherically symmetric), it has the enormous benefit that all orbits are fully analytic (Henon 1959; Eggen et al. 1962; Binney & Tremaine 2008). It is therefore an excellent tool for developing physical understanding and making qualitative predictions. We therefore choose our unperturbed potential to be $\Phi_0(r) = \Phi_\mathrm{I}(r)$.

The circular velocity in the isochrone potential obeys

$$v_\mathrm{c}^2(r) = \frac{GMr^2}{(b + a)^2 a}, \qquad a \equiv \sqrt{b^2 + r^2}. \tag{6}$$

In order to match the circular velocity of the Milky Way v_0 at the Sun's radius r_0, we choose

$$GM = \frac{v_0^2}{r_0^2}\left(b + \sqrt{b^2 + r_0^2}\right)^2 \sqrt{b^2 + r_0^2}. \tag{7}$$

Following Portail et al. (2017), we set $r_0 = 8.2$ kpc and $v_0 = 238$ km s^{-1}, and choose $b = 3$ kpc. This gives $M = 2.35 \times 10^{11} M_\odot$ and a maximum circular velocity of $v_\mathrm{max} \approx 241$ km s^{-1}. The rotation curve for this choice of parameters is shown in Fig. 1. For comparison, we also show several realistic potentials fitted to data from the Milky Way, namely those of McMillan (2017) and Portail et al. (2017), and the MilkyWayPotential from Gala (Price-Whelan 2017). The isochrone rotation curve is a reasonable match to the Milky Way at $r \gtrsim 4$ kpc, but is less realistic at smaller radii. This is partly because the isochrone potential has a homogeneous core, while cosmological dark halos have a density cusp. The circular velocity in the central regions is therefore smaller in Φ_I than in the Milky Way. We set the pattern speed of the bar to $\Omega_\mathrm{b} = 35$ km s^{-1}kpc^{-1}, close to many recent estimates for the Milky Way (e.g. Sanders et al. 2019; Binney 2020; Chiba & Schönrich 2021). With this choice of parameters the corotation radius (where $v_\mathrm{c}(r) = r\Omega_\mathrm{b}$) is $r_\mathrm{CR} = 6.87$ kpc. Throughout this paper we place the Sun at an angle relative to the bar

[1] This differs from the convention used by Collett et al. (1997), in which the resonance condition was changed for retrograde orbits so that the formulae for the l/m resonant orbit at $J_\phi > 0$ match onto the $l/m + 1$ resonant orbit at $J_\phi < 0$ (see Section 2.2).

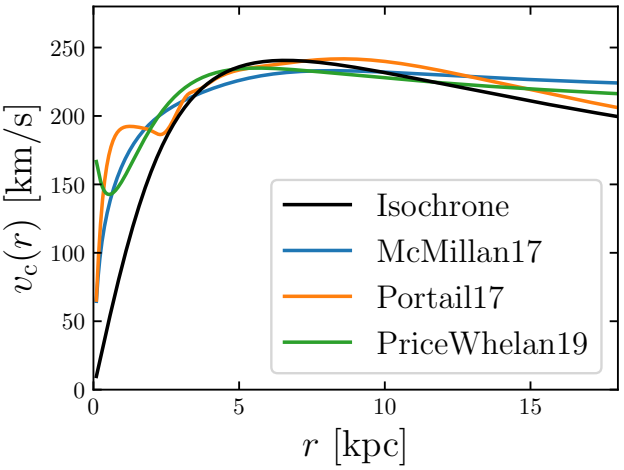

Figure 1. Circular velocity $v_c(r)$ of the isochrone potential for our choice of parameters, with three realistic Milky Way models for comparison. The mass M of the potential is chosen such that v_c matches the observed value in the Solar neighbourhood, and the selected scale radius b gives a reasonably flat rotation curve across most of the Galactic disc. Our isochrone model is a good approximation to the Milky Way for $r \gtrsim 4$ kpc, but the less concentrated central mass distribution results in a smaller $v_c(r)$ at $r \lesssim 4$ kpc.

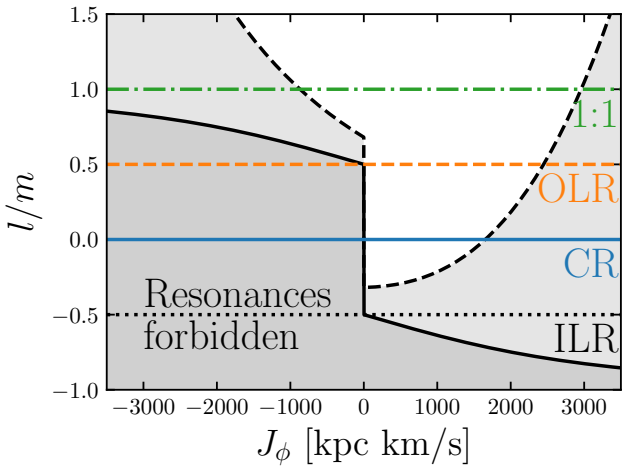

Figure 2. Minimum value of l/m required for the existence of resonant orbits in the $\theta = \pi/2$ plane as a function of J_ϕ, in the isochrone potential. Resonances are possible above the black dashed line for our choice of pattern speed Ω_b, and possible for some smaller value of Ω_b above the black solid line. Below the black solid line they are impossible for this potential in this plane. The horizontal lines mark the positions of some of the most important resonances, including the corotation (CR) and outer Lindblad (OLR) resonances. The CR and OLR are always only possible on prograde orbits ($J_\phi > 0$), but higher values of l/m are possible for $J_\phi < 0$. The inner Lindblad resonance (ILR) is not possible for this choice of potential and pattern speed. See Section 2.2 for a discussion of retrograde resonant orbits.

of $\phi_\odot - \phi_b = -30°$, consistent with the measurements of e.g. Wegg et al. (2015).

2.1 Resonances in the isochrone potential

In this section we derive the loci of bar resonances in spaces of energy E and radial action J_r versus azimuthal action J_ϕ. We utilise the property of the isochrone potential that the Hamiltonian and all actions and frequencies can be written as analytic functions of each other. As discussed above, this requires the approximation that the bar potential is a small perturbation, such that the true frequencies can be approximated by the unperturbed frequencies Ω_i.

Following Binney & Tremaine (2008), we express the actions in spherical coordinates (r, θ, ϕ). The unperturbed Hamiltonian is

$$H_0(\boldsymbol{J}) = -\frac{(GM)^2}{2\left[J_r + \frac{1}{2}\left(L + \sqrt{L^2 + 4GMb}\right)\right]^2}, \tag{8}$$

$$L \equiv J_\theta + |J_\phi|. \tag{9}$$

$J_\phi = L_z$ and L are the z-component and magnitude of angular momentum respectively. Using equation 3 the frequencies are then

$$\Omega_r = \frac{(GM)^2}{\left[J_r + \frac{1}{2}\left(L + \sqrt{L^2 + 4GMb}\right)\right]^3}, \tag{10}$$

$$\Omega_\theta = \frac{1}{2}\left(1 + \frac{L}{\sqrt{L^2 + 4GMb}}\right)\Omega_r, \tag{11}$$

$$\Omega_\phi = \mathrm{sgn}(J_\phi)\Omega_\theta. \tag{12}$$

Substituting the above frequencies into the resonance condition (equation 4) gives (e.g., Lynden-Bell 1979; Earn & Lynden-Bell 1996)

$$\left[\frac{1}{2}\left(1 + \frac{L}{\sqrt{L^2 + 4GMb}}\right)\mathrm{sgn}(J_\phi) + \frac{l}{m}\right]\Omega_r = \Omega_b. \tag{13}$$

Noticing that the Hamiltonian can be written as $H_0(\boldsymbol{J}) = -\frac{1}{2}(GM\Omega_r)^{2/3}$, we can eliminate Ω_r to obtain the energy of the (l, m) resonance as a function of J_ϕ and L. We can also find the radial action J_r. From equation 10, this is

$$J_r = \left[\frac{(GM)^2}{\Omega_r}\right]^{\frac{1}{3}} - \frac{1}{2}\left(L + \sqrt{L^2 + 4GMb}\right). \tag{14}$$

The energy and radial action along the (l, m) resonance are therefore:

$$E_{(l,m)} = -\frac{1}{2}(GM\Omega_b)^{\frac{2}{3}}\left[\frac{1}{2}\left(1 + \frac{L}{\sqrt{L^2 + 4GMb}}\right)\mathrm{sgn}(J_\phi) + \frac{l}{m}\right]^{-\frac{2}{3}}, \tag{15}$$

$$J_{r,(l,m)} = \left[\frac{(GM)^2}{\Omega_b}\right]^{\frac{1}{3}}\left[\frac{1}{2}\left(1 + \frac{L}{\sqrt{L^2 + 4GMb}}\right)\mathrm{sgn}(J_\phi) + \frac{l}{m}\right]^{\frac{1}{3}} - \frac{1}{2}\left(L + \sqrt{L^2 + 4GMb}\right), \tag{16}$$

subject to the conditions,

$$\frac{l}{m} > -\frac{1}{2}\left(1 + \frac{L}{\sqrt{L^2 + 4GMb}}\right)\mathrm{sgn}(J_\phi), \tag{17}$$

$$\frac{l}{m} \geq \frac{\Omega_b}{(GM)^2}\left[\frac{1}{2}\left(L + \sqrt{L^2 + 4GMb}\right)\right]^3 - \frac{1}{2}\left(1 + \frac{L}{\sqrt{L^2 + 4GMb}}\right)\mathrm{sgn}(J_\phi). \tag{18}$$

The first condition is required so that $\Omega_r > 0$, and applies equally for all bar pattern speeds. The second ensures that $J_{r,(l,m)} \geq 0$, and depends on the pattern speed Ω_b. If equations (17) and (18) are not satisfied for particular choices of J_ϕ, L and Ω_b, then the (l, m) resonant orbit cannot exist in our isochrone potential for those values.

Note that for $\Omega_b > 0$, equation 17 is always satisfied if equation (18) is satisfied. The first condition represents the hard minimum of l/m in the limit $\Omega_b \to 0$.

In Fig. 2, we plot the minimum l/m for resonance against J_ϕ for orbits in the $\theta = \pi/2$ plane. The solid and dashed black lines indicate the constraints from equations (17) and (18) respectively. For the outer Lindblad resonance (OLR, $l/m = 1/2$) and below, resonant orbits are only ever possible for $J_\phi > 0$. However, resonances are still possible for some retrograde orbits at higher l/m.

Using equations (15) and (16), we show the locations of a series of resonances in energy vs angular momentum space (J_ϕ, E) and action space (J_ϕ, J_r) in Fig. 3. These are the most important resonances, with $m = 2$ and $l \in \{0, 1, 2, 3, 4\}$. This set includes the corotation resonances (CR, $l/m = 0$) and the outer Lindblad resonance (OLR, $l/m = 1/2$). For our choice of parameters, the inner Lindblad resonance (ILR, $l/m = -1/2$) does not exist in the isochrone potential. However, it does exist for smaller values of Ω_b, when the black dashed line in Fig. 2 would be at lower l/m. As J_ϕ decreases from its maximum value, the energy of each resonance decreases. This is because at fixed energy Ω_ϕ decreases as J_ϕ decreases. Equation 4 dictates that in order to remain in the resonance, Ω_r must therefore increase to compensate. Hence, E decreases as J_ϕ is reduced along each resonance. In (J_r, J_ϕ) space, the resonances are approximately straight lines for small J_r, as previously shown (e.g., Collett et al. 1997; Sellwood 2010; Trick et al. 2021).

2.2 Retrograde orbits

The equations above are all valid for both prograde and retrograde orbits. However, the orbit on a given (l, m) resonance changes discontinuously as the sign of J_ϕ is changed. Each prograde resonance is continuous in E and J_r with a prograde resonance with a different value of l. For example, as expected from equation 17 and Fig. 2, the CR and OLR exist only at $J_\phi > 0$, but are continuous with higher resonances at $J_\phi < 0$. Generally, each l/m resonant orbit at $J_\phi > 0$ is related to the $l/m + 1$ resonant orbits at $J_\phi < 0$. The continuity between these resonances on each side of $J_\phi = 0$ was noted earlier (e.g., Kalnajs 1977; Collett et al. 1997), and can be understood intuitively by plotting the orbits in configuration space. In Appendix A, we give equations relating the angle variables θ_i to the physical coordinates of particles on given orbits (r, ϕ). We use these equations to plot the orbits of the $l/m = 0$ and $l/m = 1$ resonances for $J_\phi = \pm 200$ kpc km s^{-1} in Fig. 4. The left-hand column shows the inertial frame, and the right-hand column shows the frame co-rotating with the bar (i.e. rotating at frequency Ω_b).

The orbits in the inertial frame are all qualitatively similar, consisting of highly eccentric motion around a curve whose apocentres and pericentres precess by some angle per radial period. The apocentric radii of the prograde $l/m = 0$ and retrograde $l/m = 1$ orbits are similar, while that of the prograde $l/m = 1$ orbit is much greater, as expected from the higher energy.

The right-hand column is more informative. Let ϕ' be the angle measured from the X-axis in this frame (i.e. $\tan\phi' = Y/X$). For the CR ($l/m = 0$) orbit, notice the Galactic centre is not enclosed by the orbit, so ϕ' oscillates about a certain value instead of circulating through all possible values. This is why the orbit is in corotation, with $\Omega_\phi = \Omega_b$. Now consider reducing the angular momentum J_ϕ of the orbit. The pericentre decreases until it reaches zero at $J_\phi = 0$. If J_ϕ continues to become negative, the pericentre crosses to the opposite side of the origin, such that the Galactic centre is now enclosed. This is the case seen in the middle row. Now ϕ' circulates between 0 and

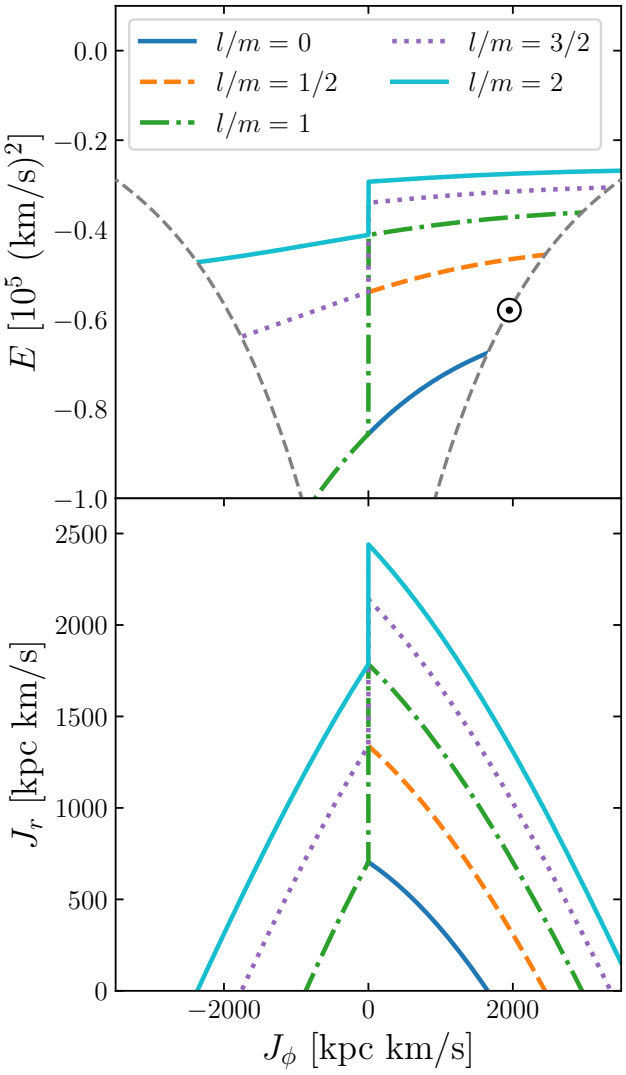

Figure 3. Top panel: Energy E vs z-angular momentum $L_z = J_\phi$ for a series of resonances. Each colour corresponds to a different resonance as marked in the legend. The grey dashed lines mark the loci of circular orbits in the $\theta = \pi/2$ plane, with a circular orbit at the Sun's radius r_0 marked with the $\odot$ symbol. **Bottom panel:** As above, but showing radial action J_r vs J_ϕ.

2π in the same time as one radial period. Therefore $\Omega_\phi - \Omega_b = \Omega_r$, and $l/m = 1$. In the same way any prograde l/m resonant orbit matches onto a retrograde $l/m + 1$ orbit.

Meanwhile, the prograde $l/m = 1$ orbit also circulates in ϕ' once per radial period, but the frequencies are considerably slower. This is because the orbital motion is in the same sense as the bar's rotation, so the magnitude of the relative frequency $|\Omega_\phi - \Omega_b|$ is smaller.

2.3 Particle dynamics near resonance

So far we have neglected the effects of the bar itself, considering only the exact resonances of an infinitesimal perturbation rotating with some pattern speed. We must now address its influence on orbits close to the resonances, as this will determine their stability. This can tell us, for example, which orientations of resonant orbits relative to the bar are possible. We follow the method outlined by

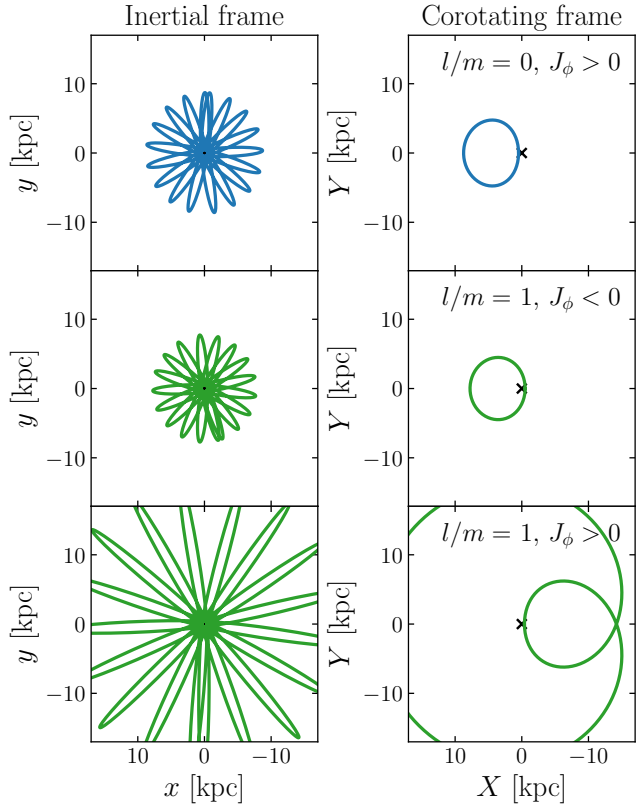

Figure 4. Shapes of the $l/m = 0$ and $l/m = 1$ resonant orbits with $|J_\phi| = 200$ kpc km s^{-1}, in the inertial frame (left-hand column) and the frame corotating with the bar (right-hand column). The $l/m = 1$ resonance is shown for both $J_\phi < 0$ (middle row) and $J_\phi > 0$ (bottom row). Note that the X-axis is flipped, such that the bar rotates in a clockwise sense. The Galactic centre is marked by the black crosses. The orientations of the orbits in the (X, Y) frame are arbitrarily chosen.

Tremaine & Weinberg (1984) and others (e.g. Binney 2018; Chiba et al. 2021; Hamilton et al. 2023), considering a steadily rotating bar with pattern speed Ω_b. Following Chiba et al. (2021), we set the potential of the bar perturbation in the $\theta = \pi/2$ plane to

$$\Phi_\mathrm{b}(r, \phi, t) = \Phi_2(r) \cos\left[2(\phi - \Omega_\mathrm{b} t)\right], \tag{19}$$

$$\Phi_2(r) = -A \frac{r^2}{[r_\mathrm{b} + r]^5}, \tag{20}$$

where r_b is the scale length of the bar and A is a positive constant. This is a quadrupole perturbation with an azimuthal minimum lying parallel to $\phi = \Omega_\mathrm{b} t \equiv \phi_\mathrm{b}$, the major axis of the bar. We set $r_\mathrm{b} = 1.9$ kpc. This is approximately equal to $0.28\, r_\mathrm{CR}$, following Chiba et al. (2021) and Hamilton et al. (2023).

For a particle orbiting close to the (l, m) resonance, define the slow angle,

$$\theta_\mathrm{s} \equiv l\theta_r + m(\theta_\phi - \phi_\mathrm{b}) \tag{21}$$

$$= l\theta_r + m(\theta_\phi - \Omega_\mathrm{b} t), \tag{22}$$

which evolves with frequency

$$\Omega_\mathrm{s} \equiv \dot{\theta}_\mathrm{s} = l\Omega_r + m(\Omega_\phi - \Omega_\mathrm{b}). \tag{23}$$

We see from equation 4 that near the (l, m) resonance this frequency will be much smaller than Ω_ϕ and Ω_r. We also define the fast angle θ_f, choosing it to be equal to the radial angle:

$$\theta_\mathrm{f} \equiv \theta_r. \tag{24}$$

We wish to make a canonical transformation from the original angle-action variables $(\boldsymbol{\theta}, \boldsymbol{J})$ to a new set $(\boldsymbol{\theta'}, \boldsymbol{J'})$, where $\boldsymbol{\theta'} \equiv (\theta_\mathrm{f}, \theta_\mathrm{s})$ and $\boldsymbol{J'} \equiv (J_\mathrm{f}, J_\mathrm{s})$. This will allow us to separate the orbital motion into fast $(\theta_\mathrm{f}, J_\mathrm{f})$ and slow $(\theta_\mathrm{s}, J_\mathrm{s})$ components.

We use the generating function (e.g., Lynden-Bell 1973; Collett et al. 1997)

$$W(\boldsymbol{\theta}, \boldsymbol{J}, t) = \left[l\theta_r + m(\theta_\phi - \Omega_\mathrm{b} t)\right] J_\mathrm{s} + \theta_r J_\mathrm{f}, \tag{25}$$

which satisfies one equation required for a canonical transformation

$$\boldsymbol{\theta'} = \frac{\partial W}{\partial \boldsymbol{J'}}. \tag{26}$$

The other equations describing the transformation then tell us

$$\boldsymbol{J} \equiv (J_r, J_\phi) = \frac{\partial W}{\partial \boldsymbol{\theta}}, \tag{27}$$

$$= (lJ_\mathrm{s} + J_\mathrm{f}, mJ_\mathrm{s}), \tag{28}$$

$$H'(\boldsymbol{\theta'}, \boldsymbol{J'}, t) = H(\boldsymbol{\theta}, \boldsymbol{J}, t) + \frac{\partial W}{\partial t} \tag{29}$$

$$= H(\boldsymbol{\theta}, \boldsymbol{J}, t) - m\Omega_\mathrm{b} J_\mathrm{s}, \tag{30}$$

where H' is the perturbed Hamiltonian. The slow and fast angles are therefore $J_\mathrm{s} = J_\phi/m$ and $J_\mathrm{f} = J_r - \frac{l}{m} J_\phi$. We split the Hamiltonian into the unperturbed stationary part and a perturbation due to the bar, which we expand as a Fourier series:

$$H'(\boldsymbol{\theta'}, \boldsymbol{J'}) = H_0(\boldsymbol{J'}) + \sum_{\boldsymbol{k}} \Psi_{\boldsymbol{k}} e^{i\boldsymbol{k}\cdot\boldsymbol{\theta'}} - m\Omega_\mathrm{b} J_\mathrm{s}, \tag{31}$$

$$\boldsymbol{k} \equiv (k_\mathrm{f}, k_\mathrm{s}). \tag{32}$$

The Fourier coefficients $\Psi_{\boldsymbol{k}}$ can be expressed in terms of the potential of the bar perturbation Φ_b (see Appendix B of Chiba et al. 2021). The time dependence of the Hamiltonian has been absorbed into the slow angle θ_s (Hamilton et al. 2023). Since θ_f evolves much faster than θ_s, we may average over θ_f to obtain:

$$\bar{H}'(\theta_\mathrm{s}, \boldsymbol{J'}) = H_0(\boldsymbol{J'}) + \sum_{k_\mathrm{s}} \Psi_{k_\mathrm{s}} e^{ik_\mathrm{s}\theta_\mathrm{s}} - m\Omega_\mathrm{b} J_\mathrm{s}, \tag{33}$$

$$\Psi_{k_\mathrm{s}} \equiv \Psi_{(0,k_\mathrm{s})}. \tag{34}$$

For the important resonances for which $m = 2$ (including all those shown in Fig. 3), only $k_\mathrm{s} = \pm 1$ terms contribute to the sum (Chiba et al. 2021). The Hamiltonian must also be real, implying that

$$\bar{H}'(\theta_\mathrm{s}, \boldsymbol{J'}) = H_0(\boldsymbol{J'}) + 2\Psi_1(\boldsymbol{J'}) \cos\theta_\mathrm{s} - m\Omega_\mathrm{b} J_\mathrm{s}, \tag{35}$$

where we have used the fact that Ψ_1 is real, as shown by Chiba et al. (2021):

$$\Psi_1(\boldsymbol{J'}) = \frac{1}{2\pi} \int_0^\pi \mathrm{d}\theta_r \Phi_2(r) \cos\left[2\left(\phi - \theta_\phi - \frac{l}{m}\theta_r\right)\right]. \tag{36}$$

Hamilton's equations then give (e.g., Lynden-Bell 1979; Collett et al. 1997)

$$\dot{J}_\mathrm{s} = -\frac{\partial \bar{H}'}{\partial \theta_\mathrm{s}} = 2\Psi_1 \sin\theta_\mathrm{s}, \tag{37}$$

$$\dot{\theta}_\mathrm{s} = \frac{\partial \bar{H}'}{\partial J_\mathrm{s}} = \frac{\partial H_0}{\partial J_\mathrm{s}} + 2\frac{\partial \Psi_1}{\partial J_\mathrm{s}} \cos\theta_\mathrm{s} - m\Omega_\mathrm{b}. \tag{38}$$

We differentiate equation 38 and substitute in equation 37. Discarding

small terms containing $O(\Psi_1^2)$ or $\dot{\theta}_s$ gives the pendulum equation (e.g., Lynden-Bell 1973; Chirikov 1979; Collett et al. 1997),

$$\ddot{\theta}_s = 2G\Psi_1 \sin\theta_s, \tag{39}$$

$$G \equiv \frac{\partial^2 H_0}{\partial J_s^2}. \tag{40}$$

The quantity G is sometimes called the 'cooperation parameter' (Earn & Lynden-Bell 1996) or the 'inertial response' (Collett et al. 1997).

We are interested in the implications of this equation for the stability of resonant orbits. Let $\theta_{s,res}$ be the stable equilibrium point of θ_s as given by equation 39. This depends on the sign of $G\Psi_1$:

$$\theta_{s,res} = \begin{cases} 0, & G\Psi_1 < 0 \\ \pi, & G\Psi_1 > 0. \end{cases} \tag{41}$$

We can relate $\theta_{s,res}$ to the orientations of the stable resonant orbits by evaluating equation 21 at a pericentre, where $\theta_r = 0$ and $\theta_\phi = \phi$. Hence $\theta_{s,res} = m(\phi - \phi_b)$. For the $m = 2$ resonances this gives us the locations of the stable pericentres relative to the bar:

$$\phi_{peri} - \phi_b = \begin{cases} 0, \pi, & G\Psi_1 < 0 \\ \pm\frac{\pi}{2}, & G\Psi_1 > 0. \end{cases} \tag{42}$$

We calculate G analytically for the isochrone potential in Appendix B. For most of the orbits we consider, $G < 0$. However, the sign of Ψ_1 depends on the orbit. For example, consider a prograde low-eccentricity orbit at the corotation resonance, $l = 0$. Near a circular orbit $\phi - \theta_\phi$ is small, so the cosine in the integrand of equation 36 will always be positive. Since $\Phi_2(r) < 0$ by definition (equation 20), $\Psi_1 < 0$ for this orbit. Therefore $\phi_{peri} - \phi_b = \pm\pi/2$, and the orbit will be centred on the bar's L_4 and L_5 Lagrange points. This is the result expected for low-eccentricity orbits (e.g. see Section 3.3.2 in Binney & Tremaine 2008).

Now consider a very highly eccentric prograde orbit, still with $l = 0$. As the particle moves away from its pericentre, ϕ will increase by $\sim \pi/2$ very rapidly as the orbit passes close to the origin. However, θ_ϕ will increase much more slowly, at a uniform rate throughout the orbit. This will result in $\phi - \theta_\phi$ being closer to $\pi/2$ than 0, so the cosine will be negative for this part of the orbit. Since the weighting by $\Phi_2(r)$ is greatest for small r, this section of the orbit may be able to dominate the integral and cause Ψ_1 to be positive. In this case $\phi_{peri} - \phi_b = 0$ or π. For this to occur, the bar's scale length r_b must be sufficiently short that the small-θ_r part of the integral dominates. Similar arguments can be applied to higher resonances with $l > 0$.

We therefore expect that, depending on the length of the bar, the angles of the resonant orbits' pericentres may flip from the bar's minor axis to its major axis as their angular momentum is reduced. We can test this prediction by using our analytic expression for G (equation B9) and numerically integrating equation 36 for a range of orbits. We use the equations in Appendix A to convert between the angles (θ_r, θ_ϕ) and the physical position (r, ϕ).

For the resonances shown in Fig. 3, we calculate the product $G\Psi_1$ across a grid of orbits in the $\theta = \pi/2$ plane with a range of J_ϕ. The results are shown in Fig. 5.

The behaviour of $G\Psi_1$ is generally in line with the above predictions. For large positive J_ϕ, $G\Psi_1 > 0$ and therefore $\phi_{peri} - \phi_b = \pm\pi/2$. This corresponds to the orbits being centred on the L_4 or L_5 Lagrange points. However, when $J_\phi \lesssim 500$ kpc km s^{-1} the sign of $G\Psi_1$ changes to negative. Hence for highly eccentric and retrograde resonant orbits, the stable pericentres are at $\phi_{peri} - \phi_b = 0$ and π, along the major axis of the bar. In this case, the orbits will be centred on the L_1 or L_2 Lagrange points. The value of J_ϕ at which the sign flips depends on the resonance, with the threshold at higher J_ϕ for larger l/m. It also depends on the scale length of the bar r_b, for the reasons discussed above. We find that the CR ($l/m = 0$) changes sign for some positive J_ϕ for all $r_b \lesssim 6$ kpc. This range includes all realistic lengths of the Milky Way's bar, so it is reasonable to expect that this sign change occurs in reality.

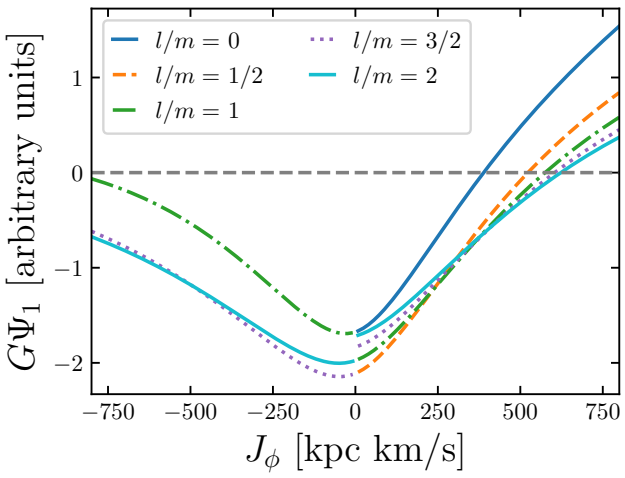

Figure 5. $G\Psi_1$ as a function of J_ϕ along the same series of resonances as Fig. 3. As J_ϕ decreases below $\approx 400 - 600$ kpc km s^{-1}, $G\Psi_1$ becomes negative. This results in the locations of the stable pericentres switching to the major axis of the bar.

We note that this result is a simplification in the limit of a weak bar, when the resonant orbits have the same energies for all orientations. If the bar is stronger, the energies of the orbits at different pericentric orientations will bifurcate: one will have slightly larger E at a given J_ϕ. The ranges of stability of these two orbits can also overlap, with both being stable at a particular angular momentum. Moreno et al. (2021) give a full treatment and calculate the stability of resonant orbits. Their Fig. 2 shows how the stability depends on the Jacobi integral E_J, a proxy for J_ϕ at a given energy. However, Moreno et al. (2021) is in agreement with our fundamental result: near-circular resonant orbits are stable with $\phi_{peri} - \phi_b = \pm\pi/2$, and near-radial orbits with $\phi_{peri} - \phi_b = 0, \pi$.

2.4 Radial phase space of resonant orbits

We are now in a position to predict the observed appearance of the radial phase space (r, v_r) of highly eccentric resonant orbits, taking into consideration the stable orbital orientations relative to the bar derived above. The radial velocity v_r and radius r of the (l, m) resonant orbit are related by

$$v_r^2(r; L, J_\phi) = 2\left[E_{(l,m)}(L, J_\phi) - \Phi_I(r)\right] - \frac{L^2}{r^2}, \tag{43}$$

where $E_{(l,m)}(L, J_\phi)$ is given by equation 15. We calculate orbits in configuration and radial phase space in the $\theta = \pi/2$ plane for a range of J_ϕ. Belokurov et al. (2023) identified substructure in (r, v_r) space by isolating stars with $|L_z| < 500$ kpc km s^{-1}, so for each resonance we generate orbits in a uniform grid of J_ϕ in the range $-500 \leq J_\phi$ [kpc km s^{-1}] ≤ 500. We use the equations in Appendix A and equation 43 to compute the orbits, and choose the angles of the pericentres according to the sign of $G\Psi_1$ (see Section 2.3).

We show the resonant orbits with $|J_\phi| < 500$ kpc km s^{-1} in Fig. 6

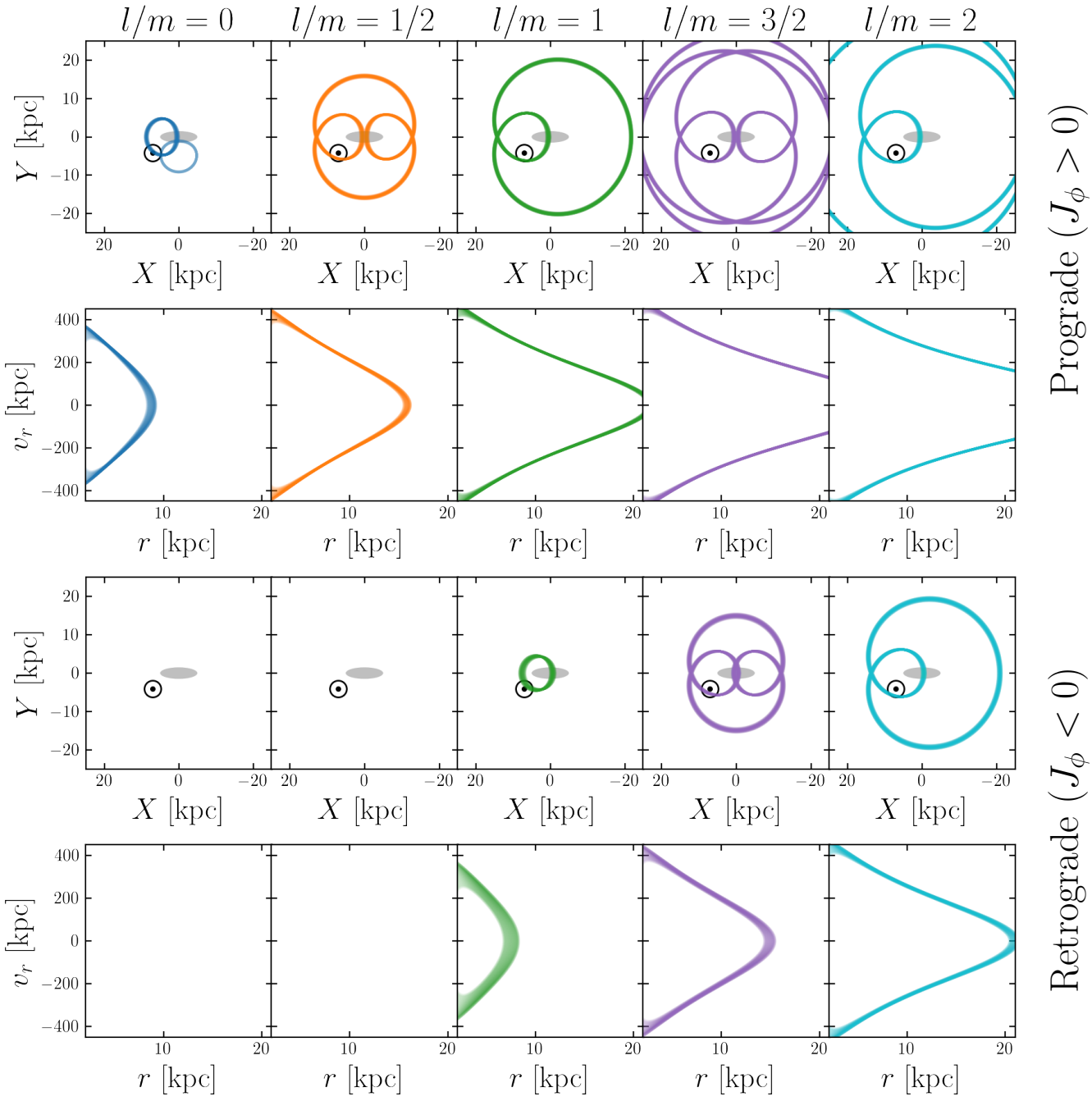

Figure 6. Resonant orbits with $|J_\phi| < 500$ kpc km s^{-1} in configuration space (X, Y) corotating with the bar (first and third rows) and in radial phase space (r, v_r) (second and fourth rows). Each column shows a different resonance, and the orbits are split according to whether they are prograde (top two rows) or retrograde (bottom two rows). In the X-Y projections, the bar (grey ellipse) lies along the X-axis, and the Sun is marked with $\odot$. As in Fig. 4, the X-axis is flipped such that the bar rotates clockwise. These projections are therefore as viewed from the north Galactic pole.

for $l/m \in \{0, 1/2, 1, 3/2, 2\}$, with $J_\phi > 0$ (top two rows) and $J_\phi < 0$ (bottom two rows). The first and third rows show the orbits in the $\theta = \pi/2$ plane, in the frame corotating with the bar (marked in grey). The X and Y axes are fixed to the bar's major and minor axes respectively. When there is a choice of pericentres (e.g. 0 or π), we show that which brings the orbit closest to the Sun (marked with $\odot$) in the interests of clarity. The second and fourth rows show the radial phase space, v_r vs r.

It is important to note that motion along these orbits is in a single direction. Since the orbits are highly radial and the bar rotates clockwise in the projections shown, the motion along most of each orbit (particularly around apocentre) is anticlockwise in the corotating frame. Carefully tracing the orbits in Fig. 6 will show that most stars will have negative v_r when passing close to the Sun. This happens whenever the stable pericentre lies on the bar's major axis ($\phi_{\rm peri} - \phi_{\rm b} = 0, \pi$). The only exception shown is at the CR ($l/m = 0$)

for $J_\phi \gtrsim 400$ kpc km s^{-1}, when $\phi_{\rm peri} - \phi_{\rm b} = \pm\pi/2$. In this case, resonant stars passing near the Sun will have $v_r > 0$. This matches observations of the Hercules stream, which is likely to be a result of disc stars begin trapped in the CR (Pérez-Villegas et al. 2017; D'Onghia et al. 2020). Note also that all resonant orbits pass close to the Sun, so trapped stars should easily be visible to *Gaia*.

As expected from the energy distributions (Fig. 3), higher resonances of a given J_ϕ have apocentres at larger radii. For a given l/m, the retrograde resonant orbits have smaller apocentric radii, slightly less than those of the prograde $l/m - 1$ orbits. By combining orbits in multiple resonances, we can therefore construct a series of nested chevrons like those observed by Belokurov et al. (2023). These are shown in the left-hand column of Fig. 7, split into prograde (top) and retrograde (bottom) orbits.

If we assume that the orbits are stable, the requirement that $\phi_{\rm peri} - \phi_{\rm b}$ take certain values severely restricts the orientations that the orbits can have. Any observational survey will naturally impose a spatial selection effect, resulting in most of its sample being located in the Solar neighbourhood. Hence, if we observe trapped stars on these highly eccentric resonant orbits, we can predict that the (r, v_r) chevrons will be asymmetrical, with a greater number of stars at $v_r < 0$.

We can predict the appearance of the observed radial phase space if we assume some selection function governing the number of stars in a sample as a function of Galactic position. We first take the resonant orbits with $|J_\phi| < 500$ kpc km s^{-1} calculated above, and sample them uniformly in θ_r between 0 and 4π. Since we are only considering resonant orbits with $m = 2$, this gives us a steady-state distribution of particles along each resonance. We take the same number of particles from each resonance, with equal numbers having each of the stable pericentric angles (usually 0 and π).

We calculate the heliocentric distance D for each particle, and assign a weighting $S(D)$ to roughly mimic the selection function of observational data. This can be seen as the fraction of stars at a particular distance which are included in the data sample. We adopt a simple form of the weighting, namely

$$S(D) \propto \exp\left(-\frac{D}{D_0}\right), \tag{44}$$

where D_0 is a scale-length. We estimate D_0 by making the simple assumption that the true spherically averaged density of stars in a thin shell of radius D centred on the Sun is independent of D. Then the number of stars between distances D and $D + \mathrm{d}D$ is $N_{\rm true}(D)\mathrm{d}D \propto D^2\mathrm{d}D$. Hence the selection function $S(D) \propto N_{\rm obs}(D)/D^2$, where $N_{\rm obs}(D)\mathrm{d}D$ is the number of observed stars in the data sample between D and $D + \mathrm{d}D$. An estimate for D_0 is obtained by plotting $\ln(N_{\rm obs}(D)/D^2)$ against D and finding the approximate gradient, which is equal to $-1/D_0$. For the data sample described in Section 4, we find that $D_0 = 1.25$ kpc is a good fit beyond distances of 2 kpc.

We apply this weighting to 2D histograms of v_r vs r for our mock stars. These are shown in the right-hand panel of Fig. 7 for prograde (top) and retrograde (bottom) particles. As expected from the discussion above, the v_r distributions in the Solar neighbourhood are asymmetric, with a greater number of stars at $v_r < 0$ on almost all resonances. The only exceptions are the CR orbits with sufficiently high J_ϕ, such that $\phi - \phi_{\rm peri} = \pm\pi/2$ (see Fig. 5). However, the asymmetry switches sign at higher radius: at $r \gtrsim 13$ kpc, there is instead a greater number of stars at $v_r > 0$. This behaviour can be understood if we examine the radial velocity as a function of position along the resonant orbits. Fig. 8 shows the orbits calculated above in the Galactic plane, with the bar and the position of the Sun marked. The colours indicate v_r, with red (blue) corresponding to

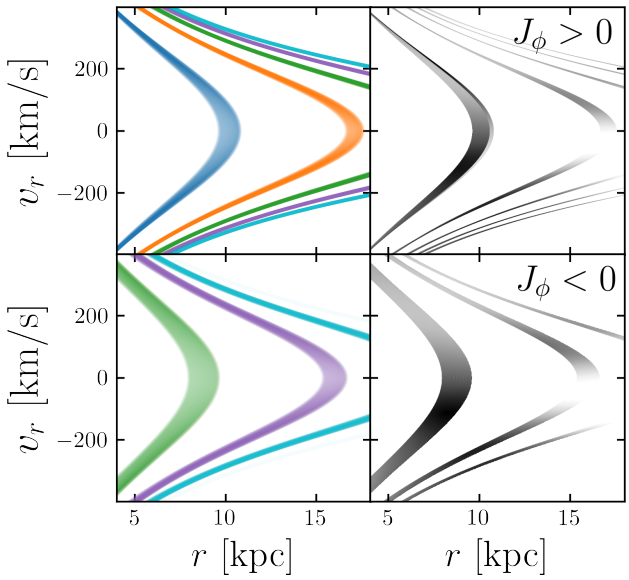

Figure 7. Radial phase space of analytic resonant orbits in the isochrone potential. The left-hand column shows each resonance colour-coded, where the colours have the same meanings as before. In the right-hand column a selection function weighting (equation 44) is applied. Darker shades correspond to higher density. On each resonance the stars are uniformly distributed in both radial angle θ_r and angular momentum J_ϕ. We split the stars into prograde (top row) and retrograde (bottom row) subsets. As expected from the shape of the orbits (Fig. 6), the chevrons are asymmetric in v_r, with higher densities of stars at $v_r < 0$ in the Solar neighbourhood.

positive (negative) values. Near the Sun, the resonant orbits mostly have $v_r < 0$, so that around $r \approx 8$ kpc the chevrons are most clearly visible there. Now consider moving from the Sun away from the Galactic centre. The branches of the orbits encountered at larger radii at the Sun's azimuth instead have $v_r > 0$. This results in the asymmetry changing sign at larger radii, as is seen in Fig. 7.

We have used our analytical model to predict the appearance of the radial phase space of highly eccentric resonant orbits in the Milky Way. In the next section we compare these predictions to the results of a test particle simulation of bar-generated chevrons.

3 TEST PARTICLE SIMULATIONS

3.1 Setup

To test the qualitative predictions of our analytical model we run a test particle simulation in a realistic Milky Way potential with a bar. We follow a similar procedure to that described in Dillamore et al. (2023), except that we use a different potential and a decelerating bar. This is expected to increase the number of stars trapped in resonances (Chiba et al. 2021), so that they will be more prominent in phase space. The setup of our simulations is summarised below and described in more detail in Appendix C.

We use the Milky Way potential fitted by Sormani et al. (2022) to the Milky Way model of Portail et al. (2017). This consists of an axisymmetric disc and three bar components. There is in addition a flattened axisymmetric dark halo and a central mass concentration (representing a nuclear stellar disc or cluster). The Solar radius and corresponding circular velocity are 8.2 kpc and 238 km s^{-1} respec-

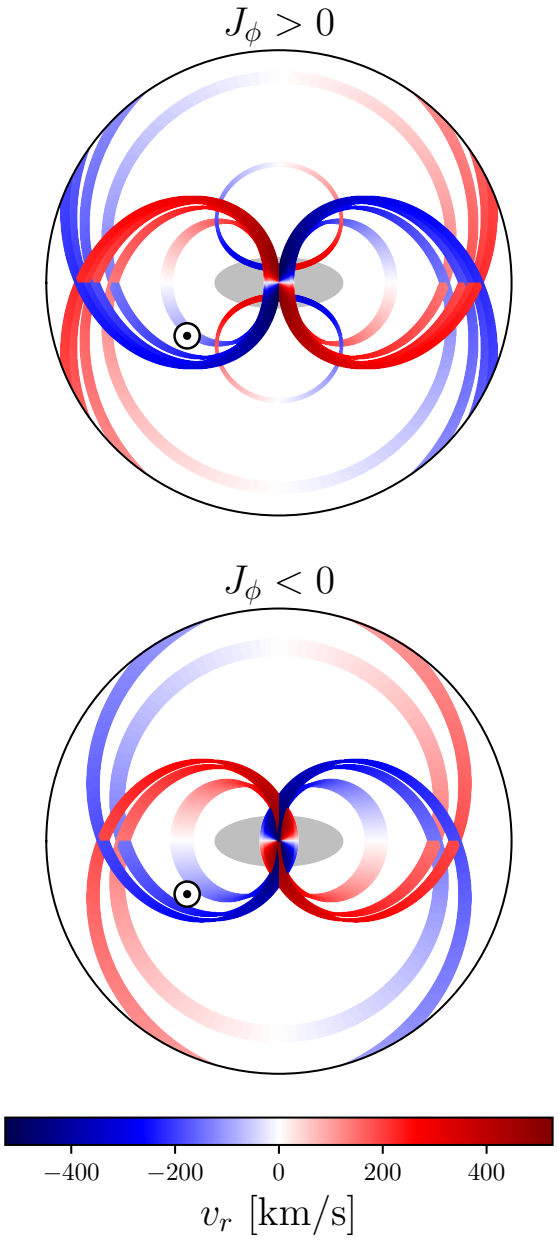

Figure 8. Resonant orbits in the Galactic plane colour-coded by radial velocity v_r, for prograde (top panel) and retrograde (bottom panel) orbits. Both circular panels have a radius of 18 kpc. The bar and position of the Sun are marked by the grey ellipse and the ⊙ symbol respectively. In the Solar vicinity the resonant orbits mostly have $v_r < 0$, but this changes at larger radii or different angles relative to the bar.

tively, as used in our analytical model. As in Section 2 we place the Sun at an angle of −30° relative to the bar.

A realistic decelerating bar should increase in length as it slows, roughly scaling with the corotation radius (e.g. Athanassoula 1992). We therefore modify the potential by changing the scale-length of its non-axisymmetric multipole components (those representing the bar). Specifically, the scale is inversely proportional to the bar's pattern speed Ω_b, and matches that of the Sormani et al. (2022) potential when $\Omega_b = 39\,\mathrm{km\,s^{-1}kpc^{-1}}$ (the pattern speed of the Portail et al. (2017) model). We leave the amplitude of these components unchanged during this scaling.

Between times $t = 0$ and $t = 2$ Gyr of the simulation we smoothly increase the strength of the non-axisymmetric components of the potential from zero to their full values. The axisymmetric components are kept constant so that the total mass is conserved. We use the same prescription for this smooth increase as Dehnen (2000) and Dillamore et al. (2023).

We set the initial pattern speed to $80\,\mathrm{km\,s^{-1}kpc^{-1}}$ and smoothly decrease it after the bar is fully grown in amplitude. Following Chiba et al. (2021) we quantify the slowing rate with the dimensionless deceleration parameter, $\eta \equiv -\dot{\Omega}_b/\Omega_b^2$. This is held constant at $\eta = 0.003$ after $t = 3$ Gyr, within the range of best-fitting values calculated by Chiba et al. (2021). The full equations governing the evolution of the bar strength and $\Omega_b(t)$ are given in Appendix C.

We initialise a distribution of stars using a steady-state distribution function (DF) in the initially axisymmetric potential. The DF $f = f_{\rm halo} + f_{\rm disc}$ consists of two components: a non-rotating spheroidal component $f_{\rm halo}$ and a flattened rotating component $f_{\rm disc}$.

The halo DF $f_{\rm halo}$ expressed as a function of the actions is derived from the spherical density profile

$$\rho_{\rm halo} \propto \left(\frac{r}{r_s}\right)^{-\gamma}\left[1+\left(\frac{r}{r_s}\right)^{\gamma-\beta}\right] \tag{45}$$

using an isotropic `QuasiSpherical` distribution function (Jeffreson et al. 2017; Vasiliev 2019). We set the inner and outer power law slopes to $\gamma = 2.3$ and $\beta = 4.6$ respectively (Deason et al. 2011), and the break radius to $r_s = 25$ kpc (Watkins et al. 2009; Deason et al. 2011; Faccioli et al. 2014; Pila-Díez et al. 2015).

The flattened rotating component is generated using the exponential DF (Vasiliev 2019),

$$\begin{aligned} f_{\rm disc}(\boldsymbol{J}) \propto \tilde{J}^3 \exp\left(-\frac{\tilde{J}}{J_{\phi,0}}\right)\exp\left(-\frac{\tilde{J}J_r}{J_{r,0}^2}\right)\exp\left(-\frac{\tilde{J}J_z}{J_{z,0}^2}\right) \\ \times\begin{cases}1 & J_\phi > 0\\ \exp\left(\frac{\tilde{J}J_\phi}{J_{r,0}^2}\right) & J_\phi < 0,\end{cases} \\ \tilde{J} \equiv |J_\phi| + J_r + 0.25J_z, \end{aligned} \tag{46}$$

where $\{J_{r,0}, J_{z,0}, J_{\phi,0}\} = \{1100, 200, 400\}$ kpc km s^{-1}. Although this is nominally a thick disc-like component, the high radial action scale $J_{r,0}$ gives us a large number of stars on highly eccentric halo-like orbits that we are interested in studying.

We integrate the orbits of the particles from the initial DF f in the evolving barred potential. We run the simulation for total time $t_f \approx 6.6$ Gyr, at which point the pattern speed is $\Omega_b = 35\,\mathrm{km\,s^{-1}kpc^{-1}}$ (as used in our analytical model).

3.2 Results

In Fig. 9 we show the energy E and radial action J_r vs the z-component angular momentum $L_z = J_\phi$ at the final snapshot of the simulation. The radial action is calculated in the axisymmetrised (i.e. azimuthally averaged) Portail et al. (2017) potential using AGAMA (Vasiliev 2019). This is analogous to Fig. 3. Indeed, in both panels there is a good match with the analytic isochrone model. In particular, in E vs J_ϕ space the ridges have roughly constant energy for $J_\phi > 0$ but tend to lower energies as J_ϕ decreases towards and below zero. Similarly, in the lower panel the ridges are steeper at $J_\phi < 0$ than their prograde counterparts. Our isochrone model therefore successfully predicts the qualitative appearance of bar resonances in integral of motion space, including the presence of retrograde resonances.

We now turn to the radial phase space. In Fig. 10 we show v_r vs r

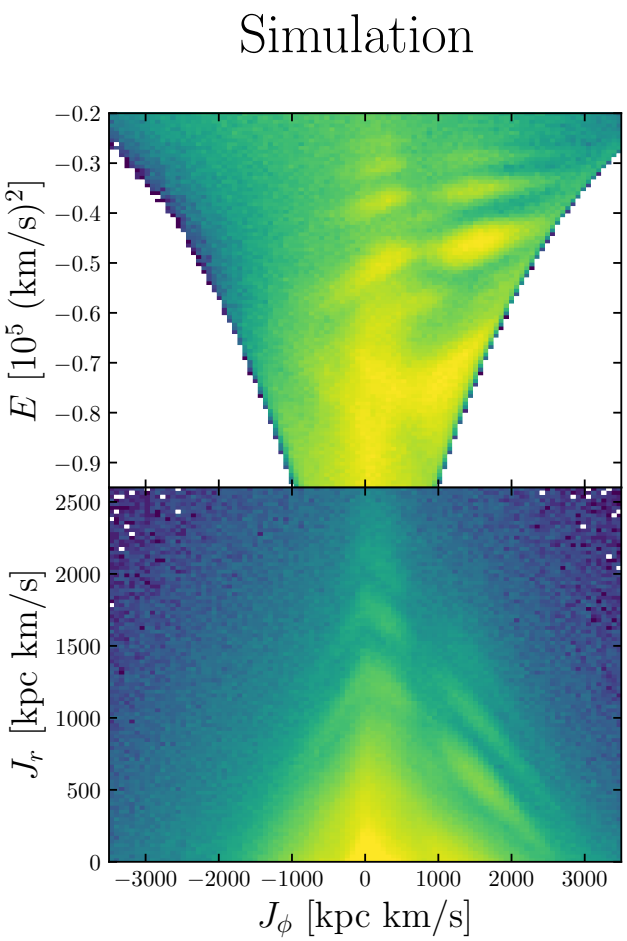

Figure 9. Energy E (top panel) and radial action J_r (bottom panel) vs J_ϕ in the simulation. In both cases the resonances are visible as overdense ridges. These have a very similar form to those shown for the analytical isochrone model in Fig. 3.

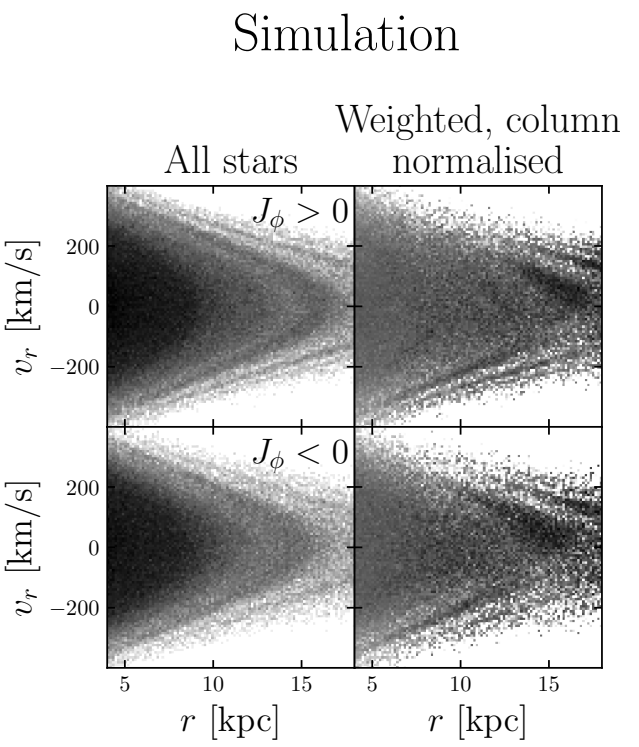

Figure 10. Radial phase space of the simulation for prograde (top row) and retrograde (bottom row) stars with $|J_\phi| < 500$ kpc km s^{-1}. The left column shows the unweighted distribution, while in the right-hand column we apply the selection effect weighting defined by equation 44. We also column-normalise the weighted histogram, such that the total count along each column of v_r bins is the same. The weighting results in the resonant chevrons becoming asymmetric in v_r.

for stars with $|J_\phi| < 500$ kpc km s^{-1}. The top and bottom rows show prograde and retrograde stars respectively. The unweighted simulation data is shown in the left-hand column. As shown by Dillamore et al. (2023) and predicted by our model in Section 2, the resonances manifest as chevron-shaped overdensities. While our simulations in Dillamore et al. (2023) only produced one clear overdensity, our setup here is able to produce multiple nested chevrons. This is due to a combination of the slowing bar and the flattened rotating component of the initial distribution function. In the prograde case (top-left panel) at least three or four different resonant chevrons are visible, which matches or exceeds the number observed in the Milky Way by Belokurov et al. (2023). Multiple resonant chevrons are also visible for retrograde orbits (bottom-left panel). Since our isochrone potential is a good match at most radii to the Portail et al. (2017) potential used in the simulations (see Fig. 1), it is possible to associate each chevron with a specific resonance by comparing with the left-hand column of Fig. 7. For example, the prograde chevron peaking at $r \approx 16$ kpc is due to the OLR ($l/m = 1/2$), and its retrograde counterpart peaking at $r \approx 15$ kpc is due to the $l/m = 3/2$ resonance.

In the right-hand column we apply the weighting defined by equation 44. The effect is similar to that predicted by the model in the right-hand column of Fig. 7: in the Solar neighbourhood ($r \sim 8$ kpc), the chevrons are only clearly visible at $v_r < 0$. The reverse is true for $r > 13$ kpc, and the peak of the OLR chevron mentioned above is most evident at $v_r > 0$.

We therefore see that asymmetry in v_r is a natural consequence of observing chevrons generated by bar resonances in some volume-limited region. The above analysis also provides us with a test: if the chevrons observed in the Milky Way are formed by resonances, the v_r asymmetry should change as a function of position. This result is not predicted by the explanation of Donlon et al. (2023) for the observed asymmetry. We now proceed to study data from *Gaia* in order to test this prediction.

4 DATA

We use positions, proper motions and line-of-sight velocities from the third data release (DR3) of *Gaia* (Gaia Collaboration et al. 2016, 2023). The line-of-sight velocity measurements are provided by the Radial Velocity Spectrometer (RVS; Katz et al. 2023) We supplement these with updated estimates of parallax calculated from *Gaia* DR3 XP spectra by Zhang et al. (2023). These parallax estimates provide us with distance measurements for stars up to larger Galactic radii than those of Bailer-Jones et al. (2021), as were used by e.g. Belokurov et al. (2023), which allows us to study a wider range of the observed radial phase space. The revised distance measurements are $D = 1/\varpi$, where ϖ are the parallax estimates provided by Zhang et al. (2023).

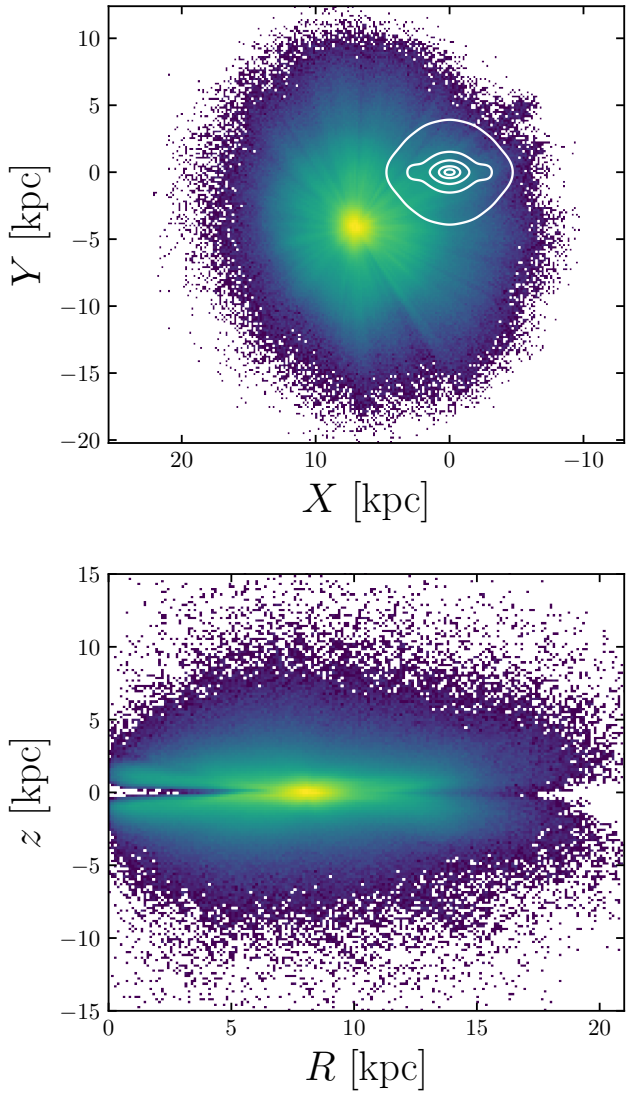

Figure 11. Spatial distributions of the data sample. **Top panel:** Face-on projection of the Galactic plane in Galactocentric Cartesian coordinates. The bar lies along the X-axis and is indicated by the white contours. **Bottom panel:** Height above the Galactic plane z versus cylindrical radius R.

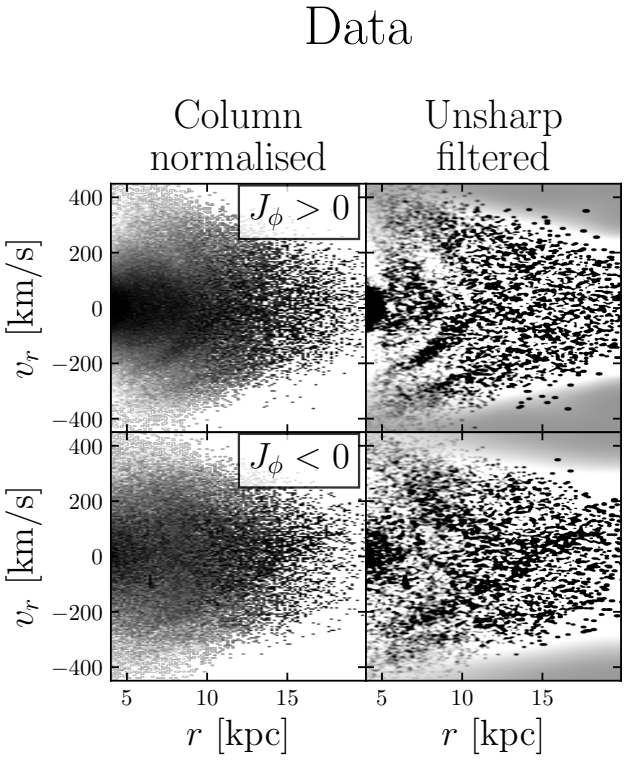

Figure 12. Radial phase space (r, v_r) of the observed data with $|J_\phi| < 500$ kpc km s^{-1}. The top (bottom) row shows prograde (retrograde) stars. In the left-hand column the data is column-normalised, such that the total count across all v_r bins in the histogram is independent of r. In the right-hand column a smooth background has been subtracted. This background was calculated by convolving the column-normalised histogram with Gaussians of standard deviation $\sigma = 8$ ($J_\phi > 0$) and 16 ($J_\phi < 0$) pixels. This unsharp masking reveals the chevrons discovered by Belokurov et al. (2023).

We apply the following cuts to clean the data sample. Following the recommendation of Zhang et al. (2023), we use only stars from their catalogue with `quality_flags` < 8. We select stars with distance uncertainties of less than 10% (i.e. $\varpi/\sigma_\varpi > 10$, where σ_ϖ is the parallax uncertainty), and distances $D < 15$ kpc. We also remove sources with an angular separation of less than 1.5° from known globular clusters within 5 kpc of the Sun.

Our final sample consists of ≈ 22 million stars with 6D phase space positions and stellar parameter estimates by Zhang et al. (2023). In order to directly compare to our model and simulations, we transform to a left-handed Galactocentric coordinate system (X, Y, z) in which the Sun is located in the Galactic plane at a distance $r_0 = 8.2$ kpc from the Galactic centre. The local standard of rest (LSR) is assumed to move on a circular orbit with velocity $v_0 = 238$ km s^{-1} (Bland-Hawthorn & Gerhard 2016), and the Sun's motion relative to the LSR is $(U, V, W)_\odot = (11.1, 12.24, 7.25)$ km s^{-1} (Schönrich et al. 2010). These match the parameters used by Portail et al. (2017). We align the X-axis (and $\phi = 0$ plane) of this coordinate system with the major axis of the bar, and place the Sun at an azimuth of $\phi_\odot = -30°$. These parameters are identical to those used in the isochrone model and simulations in Sections 2 and 3. In this left-handed coordinate system the bar rotates with positive angular frequency.

The spatial distribution of the final sample is shown in Fig. 11. The top panel shows the Galactic plane face-on, with the Sun located at $(X, Y) = (7.1, -4.1)$ kpc. Note that the X-axis is flipped such that the disc and bar rotate clockwise in this view. The white contours show the projected density of the Sormani et al. (2022) bar model for comparison. The bottom panel shows height above the plane z against cylindrical radius R. Our sample extends up to and beyond $R \approx 18$ kpc and $|z| \approx 5$ kpc, well into the halo. It also covers a wide range of Galactic azimuth ϕ.

4.1 Radial phase space

In Fig. 12 we show the density in radial phase space (r, v_r) for the subset of the data with angular momentum $|J_\phi| < 500$ kpc km s^{-1}. In the left-hand column the histograms are column-normalised, such that each r bin has the same total count across all v_r bins. The chevrons observed by Belokurov et al. (2023) are already visible as diagonal overdense striations, particularly at $J_\phi > 0$ and $v_r < 0$. Following Belokurov et al. (2023), in the right-hand column we

apply unsharp masking to reveal this finer structure. We first convolve the histograms with Gaussians with standard deviations of 8 pixels (prograde) and 16 pixels (retrograde) along r and v_r, then subtract these from the original histograms. This process reveals the chevrons more clearly, with at least two being visible for both prograde and retrograde stars.

While the shape of the chevrons resembles those produced by highly radial merger events (Dong-Páez et al. 2022; Davies et al. 2023b,a; Donlon et al. 2023), there is also a striking asymmetry in v_r, particularly at $J_\phi > 0$. While the chevrons can clearly can be seen at $v_r < 0$, they are virtually invisible at $v_r > 0$. The presence of v_r asymmetry was previously noted by Belokurov et al. (2023) and used by Donlon et al. (2023) as evidence that the prograde chevrons are dynamically young. This is because chevrons from a recent merger reach a maximum radius at a positive value of v_r (Dong-Páez et al. 2022), so are asymmetrical in v_r.

However, this is not what is observed in the Milky Way. While the chevrons in the top-right panel of Fig. 12 are indeed asymmetric, they are barely visible at $v_r > 0$. This is not what is expected from asymmetric dynamically young chevrons, which are similarly overdense at both positive and negative v_r (e.g. see Fig. 2 in Donlon et al. 2023). The observed asymmetry appears to be of a different nature.

However, the observed radial phase space does resemble that predicted by our bar resonance model in Figs. 7 and 10. As seen in the weighted distributions from the simulation (Fig. 10, right-hand column), little or no substructure is observed at $v_r > 0$ in the Solar neighbourhood ($r \approx 4 - 12$ kpc). This is also consistent with the analytic isochrone model, in which we predicted that around the Solar radius the chevrons would be more prominent at $v_r < 0$. However, the most prominent retrograde chevron is more symmetric, as previously noted by Donlon et al. (2023).

On first inspection the observed chevrons match the predictions for resonance-generated chevrons, at least for prograde stars. In the next section we directly compare the analytic predictions, simulation and observations in more detail.

5 ANALYSIS

We have so far presented the radial phase space of the analytic isochrone model, the simulations and the data. We have shown that asymmetry in v_r is a characteristic feature of resonant chevrons, and that this is also seen in the data. We now use this asymmetry to more closely investigate the chevrons in various projections of phase space. We also associate the chevrons with specific resonances.

5.1 Integral of motion space

We calculate the energy E and actions J_ϕ and J_r of stars in the data sample using AGAMA. As in the simulations, we use the axisymmetrised Sormani et al. (2020) potential. In Fig. 13 we show energy E (top row) and radial action J_r (bottom row) vs J_ϕ for the isochrone model, the simulation and the data. We have coloured each pixel with the mean radial velocity v_r of all stars in that pixel. In the case of the isochrone model and simulation, this is the weighted mean where equation 44 has been used as the weighting. We also calculate the actions J_r of the CR, OLR and 1:1 resonant orbits in the Galactic plane by numerically solving equation 4 at a range of J_ϕ values. As in the isochrone model and simulation, we set the pattern speed to $\Omega_b = 35\ \mathrm{km\,s^{-1}kpc^{-1}}$. The loci of these resonances are marked by black dashed lines. We also calculate the approximate actions and energies of the Hercules stream assuming velocities of $(v_r, v_\phi) = (30, 188)\ \mathrm{km\,s^{-1}}$ (Antoja et al. 2008), and indicate these with the cross labelled with 'H' in each data panel.

Qualitatively the isochrone model and simulation show the same behaviour. As J_ϕ increases along each resonance, the mean v_r changes sign from negative (at $J_\phi \lesssim 500$ kpc km s^{-1}) to positive (up to $J_\phi \approx 2000 - 3000$ kpc km s^{-1}) then back to negative at higher J_ϕ. The change in sign at $J_\phi \approx 500$ kpc km s^{-1} can be understood from the reasoning in Section 2.3. We showed that the stable orientation of the orbit's pericentre relative to the bar changes at roughly this value of J_ϕ. Due to the shapes of the orbits this leads to the particles passing through the Solar neighbourhood having $v_r < 0$ for smaller J_ϕ and $v_r > 0$ for larger J_ϕ (e.g. see Fig. 8 for orbits with small $|J_\phi|$). The change back to a negative mean v_r occurs for the OLR and higher resonances, and is due to the shape of the orbit changing as it becomes more circular. As J_ϕ increases, the loops in the orbits (e.g. see Fig. 6, top row) become smaller, which results in the closest stars to the Sun having $v_r < 0$. The fact that disc-like orbits at the OLR have a negative average v_r has been well documented (e.g. Trick et al. 2021; Chiba et al. 2021).

A characteristic signature of prograde resonances in action space (J_r vs J_ϕ) is therefore a series of diagonal bands with negative gradient, along which the sign of the mean v_r changes from negative (J_ϕ small) to positive (J_ϕ larger). Qualitatively this is also seen in the data. The three resonances marked coincide with such bands, where the mean v_r changes from negative to positive as J_ϕ increases and J_r decreases. The value of J_ϕ at which this transition occurs is similar to the simulation for the CR and 1:1 resonances (lowest and highest dashed lines), while for the OLR (middle line) this transition occurs at a higher value of J_ϕ. These bands can also be seen in the top-right panel in the space of E vs J_ϕ.

The Hercules stream is also very close to the CR and the associated diagonal band in action space. This is unsurprising, since the Hercules stream has previously been found to be consistent with trapping in the CR at a pattern speed of $\Omega_b = 35\ \mathrm{km\,s^{-1}kpc^{-1}}$. However, this band can be traced to much lower J_ϕ and higher J_r than has been previously noted. The mean v_r also transitions from positive in the vicinity of the Hercules stream to negative at lower J_ϕ. For this pattern speed the CR lies along the whole length of this band. We can therefore directly connect the Hercules stream to much more eccentric halo-like orbits on the same resonance, but with negative mean v_r in the Solar neighbourhood.

5.2 Identification of resonances in radial phase space

We have demonstrated that for a pattern speed of $\Omega_b = 35\ \mathrm{km\,s^{-1}kpc^{-1}}$, resonances with the bar coincide with both the Hercules stream and the diagonal stripes in the action space of the data. We now return to the radial phase space of the data and compare the chevrons with the distributions of stars near the resonances. The top panel of Fig. 14 again shows the action space of the data colour-coded by mean v_r, as in the bottom-right panel of Fig. 13. We again show the approximate tracks of periodic resonant orbits in the Galactic plane, calculated in the axisymmetric potential for $\Omega_b = 35\ \mathrm{km\,s^{-1}kpc^{-1}}$. For each resonance we select stars with $|J_\phi| < 500$ kpc km s^{-1} for which $|J_r - J_{r,\mathrm{res}}(J_\phi)| < 50$ kpc km s^{-1}, where $J_{r,\mathrm{res}}(J_\phi)$ is the radial action of the resonance at J_ϕ. We show contours of the distributions of these stars in radial phase space for $J_\phi > 0$ (middle panel) and $J_\phi < 0$ (bottom panel).

In Fig. 15 we show slices of the radial phase space in the vicinity of the Sun, between $r = 7.9$ and 8.5 kpc. The top two (bottom two) panels show prograde (retrograde) stars. In the first and third panels

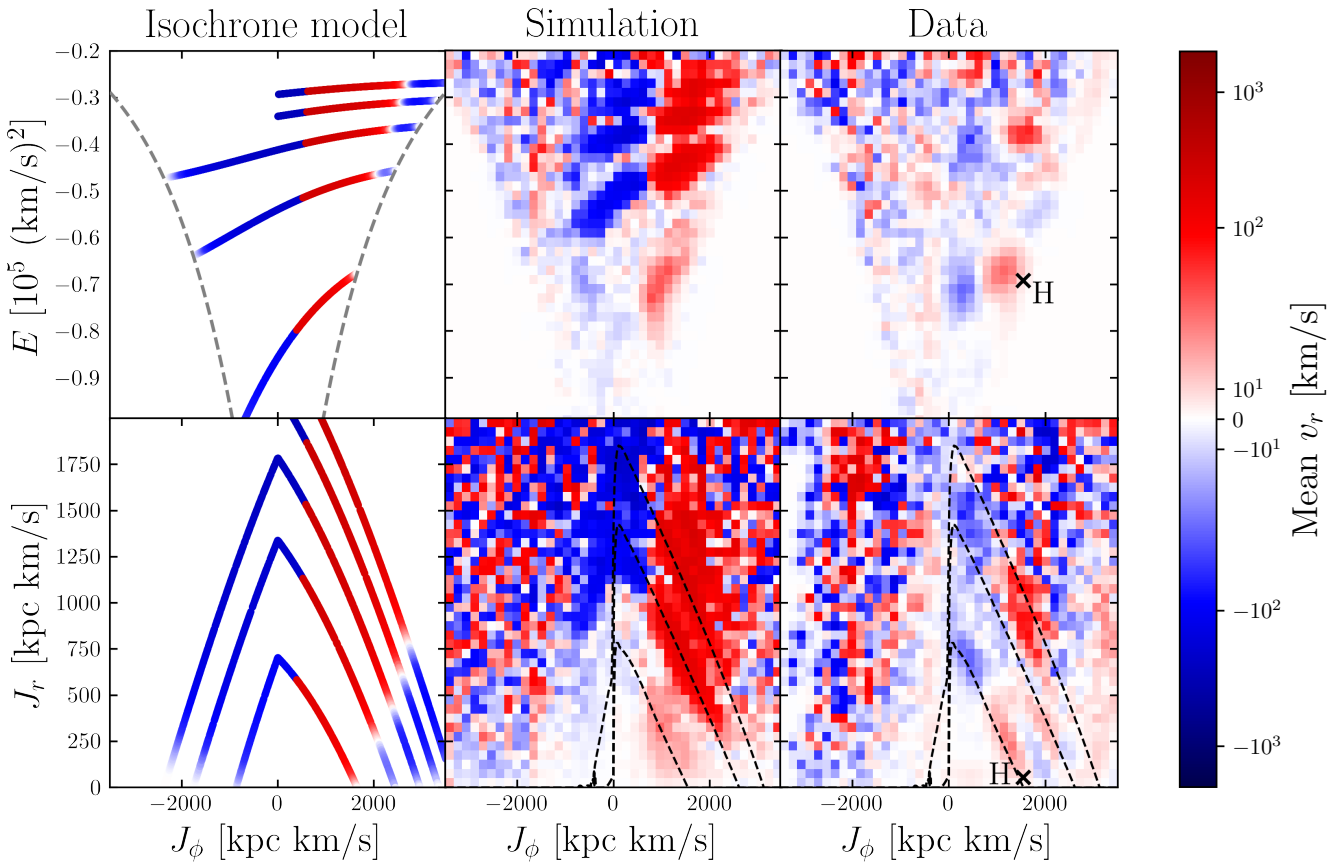

Figure 13. Energy (top row) and radial action (bottom row) versus angular momentum J_ϕ, colour coded by mean radial velocity v_r. The left-hand column shows the analytical isochrone model, the middle the simulation and the right the data. The model and simulation are both weighted according to equation 44 to mimic the selection effects of the data. The black dashed lines in the action space panels of the simulation and data mark the CR, OLR and 1:1 resonances calculated for a pattern speed of $\Omega_b = 35\,\mathrm{km\,s^{-1}kpc^{-1}}$. The crosses labelled 'H' denote the approximate location of the Hercules stream.

we show the relative difference between the distributions of v_r and a smooth background (i.e. difference divided by background). As in Figs. 12 and 14 this background is calculated by convolving the distribution with a Gaussian. The second and bottom panels show the v_r distributions of stars selected to be near the resonances, similarly to in Fig. 14.

At $J_\phi > 0$, Fig. 14 shows that the stars close to the corotation resonance (blue) coincide remarkably closely with the innermost chevron in (called Chevron 1 by Belokurov et al. 2023; Dillamore et al. 2023). The outer chevron (Chevron 3) also coincides with stars near the OLR (orange). This is confirmed in the top two panels of Fig. 15, where the strongest peaks at $v_r < 0$ ($v_r = -155\,\mathrm{km\,s^{-1}}$ and -285 $\mathrm{km\,s^{-1}}$) align almost exactly with the peaks of the CR and OLR distributions. We also mark a weaker peak ($v_r = -330\,\mathrm{km\,s^{-1}}$) which is close to the higher resonances, including $l/m = 3/2$ (purple). This weaker peak may be the same as Chevron 5 found by Belokurov et al. (2023). These strikingly close matches are strong evidence that the chevrons are indeed generated by resonances rather than a merger event.

The retrograde chevrons do not align with the $m = 2$ resonances. The most prominent (Chevron 2, peaking at $r \approx 13$ kpc) lies between the $l/m = 1$ and $l/m = 3/2$ resonances. However, we also show the $l/m = 5/4$ resonance (red), which is continuous in energy with the prograde 4:1 ultraharmonic resonance. This does match the chevron well, and their peaks are reasonably well aligned in the bottom two panels of Fig. 15 ($v_r = -200\,\mathrm{km\,s^{-1}}$). This chevron being due to an $m = 4$ resonance may also explain why it is more symmetric in v_r than the prograde chevrons. When viewed in the (X, Y) frame corotating with the bar, an $m = 4$ closed periodic orbit displays four-fold rotational symmetry with pericentres at four different values of ϕ. This means that the orbit can pass close to the Sun on multiple parts of its orbit when either $v_r > 0$ or $v_r < 0$, unlike the $m = 2$ orbits in Fig. 8. The radial phase space chevrons would therefore not be dominated by stars with $v_r < 0$.

A pair of peaks at $v_r = -285\,\mathrm{km\,s^{-1}}$ and $v_r = -310\,\mathrm{km\,s^{-1}}$ also align very closely with the $l/m = 7/4$ and $l/m = 2$ resonances respectively. However, we note that the orbits of higher resonant orbits have larger apocentres and are therefore more sensitive to the accuracy of the Galactic potential at larger radii. Since we are only considering one potential and pattern speed it is not possible to confidently associate these higher resonances with individual chevrons.

In summary, the most prominent prograde chevrons can be associated with the CR and OLR, while the clearest retrograde chevron matches the $l/m = 5/4$ resonance.

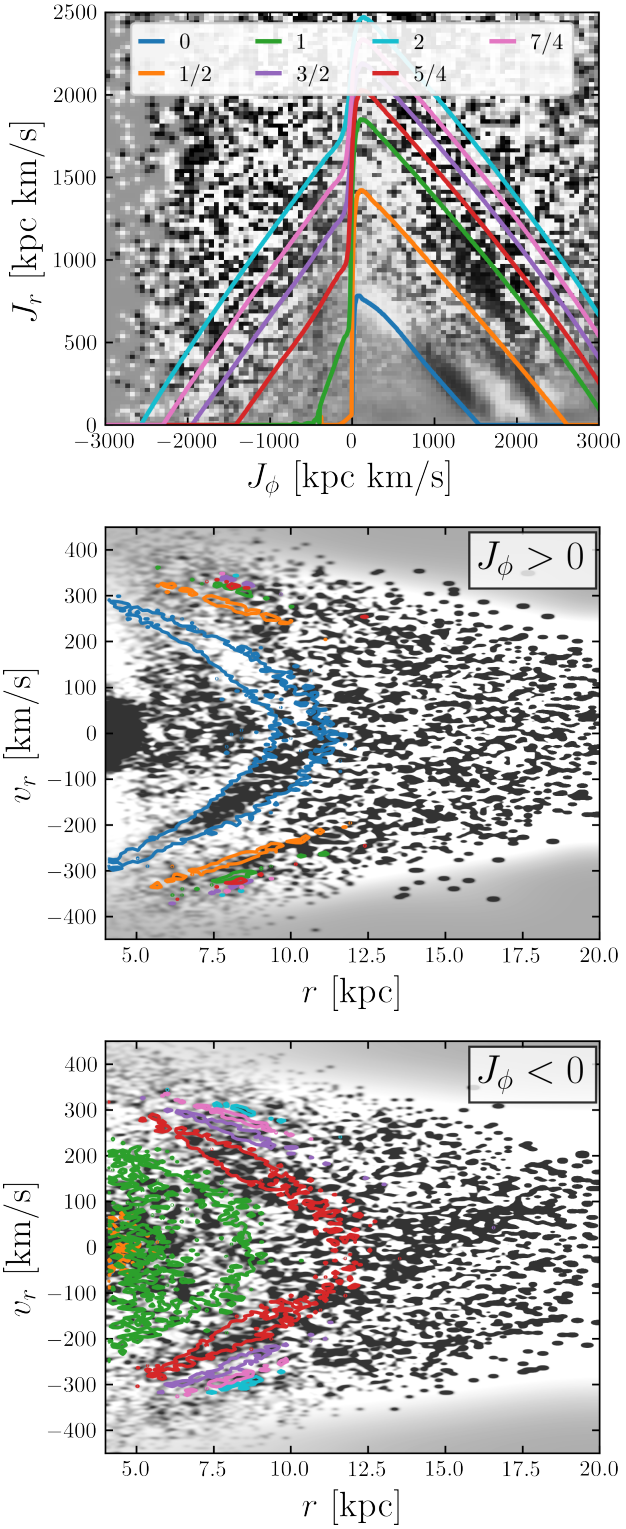

Figure 14. Top panel: a repeat of part of the bottom-right panel of Fig. 13, showing average radial velocity as a function of action. Here black (white) pixels correspond to positive (negative) mean v_r. The coloured lines indicate resonances with a bar rotating at pattern speed $\Omega_b = 35$ km s^{-1}kpc^{-1}. The numbers in the legend indicate the resonant ratio l/m. **Middle and bottom panels:** radial phase space of the data as seen in Fig. 12, for prograde (middle panel) and retrograde (right-hand panel) stars. Density contours of the selected stars near resonances are plotted on top. Some of these correspond very closely with the most prominent chevrons.

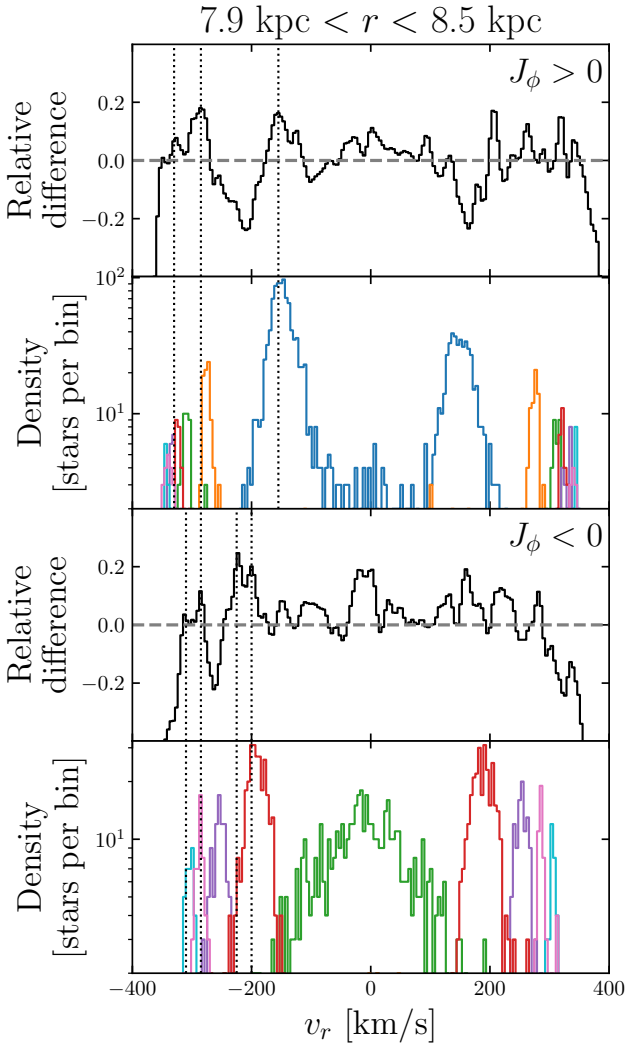

Figure 15. Distributions of v_r in the radial slice 7.9 kpc $< r <$ 8.5 kpc and $|J_\phi| < 500$ kpc km s^{-1}. The top two and bottom two panels show prograde and retrograde stars respectively. The first and third panels show the relative difference between the distribution of all stars in this slice and a smooth background (i.e. convolved with a Gaussian). The coloured histograms in the second and bottom panels show those selected close to the resonances. The colours have the same meanings as in Fig. 14. Some of the strongest peaks are marked with black dotted lines.

5.3 Asymmetry in radial phase space

As Figs. 7 and 10 show, asymmetry in v_r in radial phase space is characteristic of resonance-generated chevrons when a volume-limiting selection effect is applied to the observations. We now directly compare the asymmetry of the models and the data. Following a similar method to Donlon et al. (2023), we calculate the normalised antisymmetric component of the (r, v_r) distributions. This is defined as

$$f_{\rm anti}(r, v_r) \equiv \frac{n(r, v_r) - n(r, -v_r)}{n(r, v_r) + n(r, -v_r)}, \tag{47}$$

where $n(r, v_r)$ is the number of stars in the 2D histogram bin located at (r, v_r). This antisymmetric component is shown for the two models and the data in Fig. 16. Red (blue) indicates an excess (deficit) of stars compared to the opposite value of v_r.

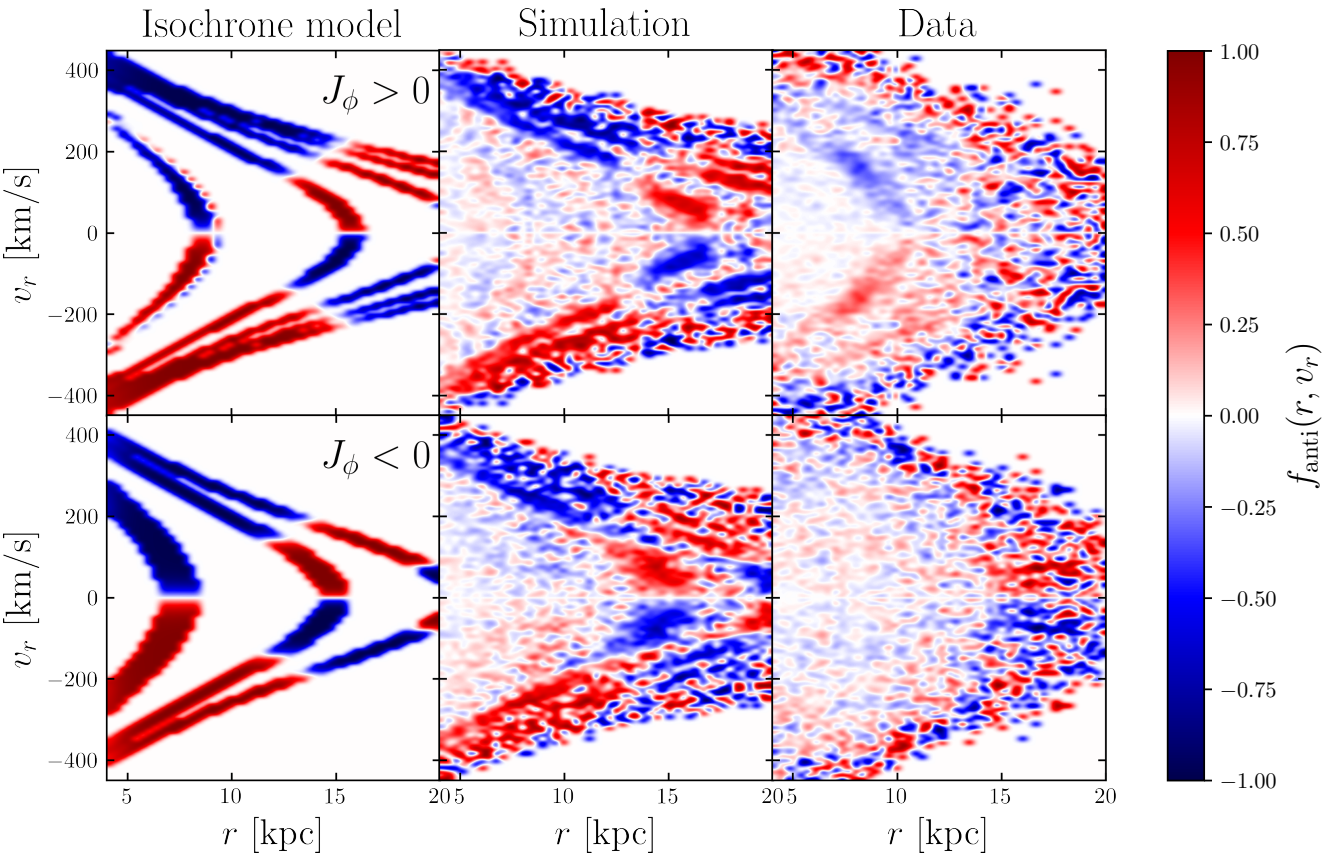

Figure 16. Antisymmetric component of the radial phase space distributions, as defined by equation 47. The left-hand, middle and right-hand columns show the analytic model, the simulation and the data respectively. The top (bottom) row shows prograde (retrograde) stars. Red (blue) indicates an excess (deficit) of stars compared to the opposite value of v_r.

For prograde stars the asymmetry previously discussed is seen as red pixels at $v_r < 0$ for $r \lesssim 13$ kpc. Both models and the data all show this effect, although we note that the corotation resonance (peaking at $r \approx 10$ kpc) is considerably fainter than the other resonances in the simulation. The outer chevron in the data (associated with the OLR) cannot be traced at $r \gtrsim 13$ kpc, due to low signal-to-noise. However, both the analytic model and the simulation make a prediction at these larger radii. As was seen in Figs. 7 and 10, the asymmetry changes sign at $r \approx 13 - 16$ kpc, with more stars in the chevrons at $v_r > 0$. This can be understood by looking at the orbits in Fig. 8. While it is not clear from our sample whether this occurs in the Milky Way, future observations may allow this prediction to be tested.

The isochrone model and simulation both predict similar effects in the retrograde stars, with the asymmetry changing sign at $r \approx 13$ kpc. However, the retrograde chevrons in the observed data do not show any significant asymmetry. Donlon et al. (2023) explained this as evidence that they result from an ancient merger whose debris has been well phase mixed. As discussed in Section 5.2, the most prominent retrograde chevron aligns reasonably well with the predicted $l/m = 5/4$ resonance, whose orbits would be expected to be more symmetric in v_r than the $m = 2$ resonances. The retrograde observations can therefore be explained by resonances if the $m = 4$ rather than $m = 2$ resonances are dominant. We note however that this does not appear to be the case in the simulation.

5.4 Asymmetry in configuration space

Fig. 16 shows that the asymmetry in v_r changes as a function of Galactic radius r. However, it must also change as a function of azimuth ϕ. In particular, Fig. 8 implies that the asymmetry changes sign if the observer's position is reflected in the major or minor axes of the bar. In Fig. 17 we show the mean v_r of stars with $|J_\phi| < 500$ kpc km s^{-1} in bins of cylindrical radius R (up to $R = 18$ kpc) and azimuth ϕ. As in Fig. 16, the columns show the analytic model, simulation and data, and the rows show prograde and retrograde stars. The bar is marked in grey, and the position of the Sun is marked with the symbol $\odot$.

The panels for the isochrone model are simply a binned version of Fig. 8, so show the behaviour described above. For both prograde and retrograde stars, the mean v_r is negative near the Sun and changes sign when moving either to larger R or across the major axis of the bar. The same effect is also seen in the simulation. We note however that the mean v_r is not perfectly antisymmetric about the bar's major axis: it is closer to zero on the opposite side from the Sun (i.e. on the leading edge of the bar). This is likely to be because the bar in the simulation is slowing with time, resulting in it lagging behind the trapped orbits in azimuth.

For prograde stars the same effect appears to be visible in the data, especially the flip in asymmetry when crossing the major axis. There is therefore reasonable agreement with the resonance origin scenario. We note that this pattern can also arise if the distances for the farthest

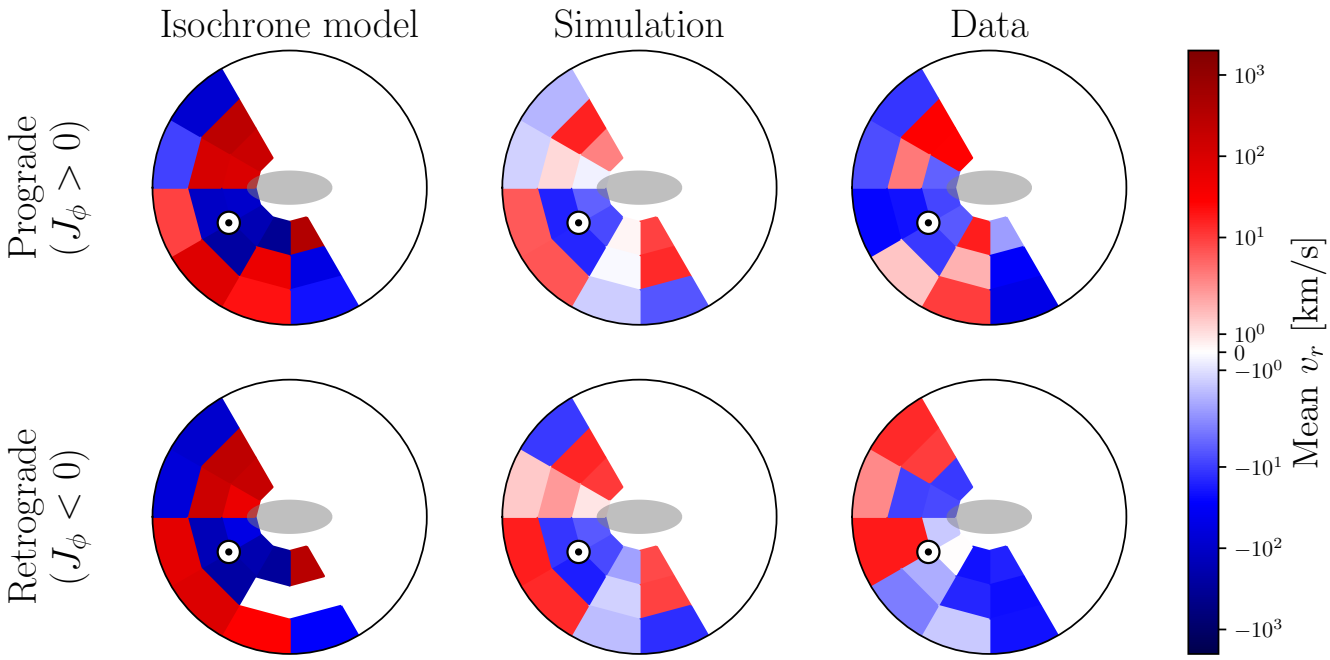

Figure 17. Mean v_r as a function of Galactic position for the isochrone model (left-hand column), the simulation (middle column) and the data (right-hand column). Each circle has a radius of 18 kpc, and the $\odot$ symbol marks the position of the Sun. The top and bottom rows show prograde (retrograde) stars. Red (blue) indicates a positive (negative) mean v_r.

stars are overestimated, so this result should be viewed with caution. As discussed in relation to Fig. 12, it is not clear whether the flip in asymmetry is visible at larger r due to low signal-to-noise. Future distance catalogues may allow a better comparison to be made.

As in the radial phase space in Fig. 16, there is weaker agreement between the data and models for the retrograde stars. While the mean v_r does become positive in the direction of the bar's major axis, this happens nearer the azimuth of the Sun than in the simulation. It is therefore not clear whether the retrograde chevrons are consistent with being bar-generated.

In the data the most prominent chevron is the one we associate with the CR, peaking at $r \approx 10$ kpc. We now consider only stars close to this chevron. Similar to the selection of stars in Fig. 14, we choose prograde stars with $|J_\phi| < 500$ kpc km s^{-1} and radial actions J_r within 100 kpc km s^{-1} of the corotation resonance (for $\Omega_\mathrm{b} = 35$ km s^{-1}kpc^{-1}). In Fig. 18 we show the fraction $f(v_r > 0)$ of these stars which have $v_r > 0$ in bins of Galactocentric azimuth ϕ. The top, middle and bottom panels show the isochrone model, simulation and data respectively. The bar's major axis lies at $\phi = \phi_\mathrm{b}$ and the Sun is at $\phi - \phi_\mathrm{b} = -30°$. As a control we also calculate $f(v_r > 0)$ for stars in the simulation and data in the complementary cuts (still $|J_\phi| < 500$ kpc km s^{-1} but with $|J_r - J_{r,\mathrm{res}}| > 100$ kpc km s^{-1}).

Both models and the data show the same qualitative trend. As previously shown, less than half the stars near this resonance have $v_r > 0$ around the Sun. This reverses on the opposite side of the bar's major axis ($\phi > \phi_\mathrm{b}$) for each model as well as the data. This can be explained by the orientations of the resonant orbits in Fig. 8. Meanwhile, the simulation and data control samples are more symmetric in v_r at all ϕ. The innermost chevron in the data is therefore qualitatively consistent with predictions for the corotation resonance as a function of ϕ.

6 CONCLUSIONS

We present a theory for the origin of the 'chevron' overdensities in the radial phase space of low-angular momentum stars in the Milky Way (Belokurov et al. 2023). We have proposed (Dillamore et al. 2023) that the chevrons are populated by stars trapped in the resonances of the Galactic bar. To investigate this hypothesis we have developed an analytic model in the isochrone potential (Henon 1959; Eggen et al. 1962), in which all orbits, integrals of motion and frequencies can be written analytically. Alongside this, we run a test particle simulation of a stellar halo in a realistic Milky Way potential with a slowing rotating bar. We compare the predictions of the model and simulation to observations from *Gaia*, supplemented by distance estimates by Zhang et al. (2023). The principal features of our model and our conclusions are summarised below.

(i) The resonant orbits with low angular momentum combine to form a series of nested overdensities in radial phase space (r, v_r). The shapes of these are similar to the chevrons formed by highly radial merger events and to those discovered in the Milky Way by Belokurov et al. (2023).

(ii) The orientations of the stable $m = 2$ resonant orbits with respect to the bar change as a function of angular momentum J_ϕ. On disc-like orbits at high J_ϕ, the pericentres of the stable orbits are aligned with the minor axis of the bar. At low angular momentum ($J_\phi \lesssim 500$ kpc km s^{-1}), the stable orientations rotate by 90° and the pericentres become aligned with the bar's major axis.

(iii) The stable resonant orbits at low J_ϕ have Galactocentric radial velocity $v_r < 0$ when they pass through the Solar neighbourhood. This means that when a sample of stars on highly eccentric orbits is viewed from the Sun, chevrons corresponding to bar resonances are predicted to be considerably more populated at $v_r < 0$. This

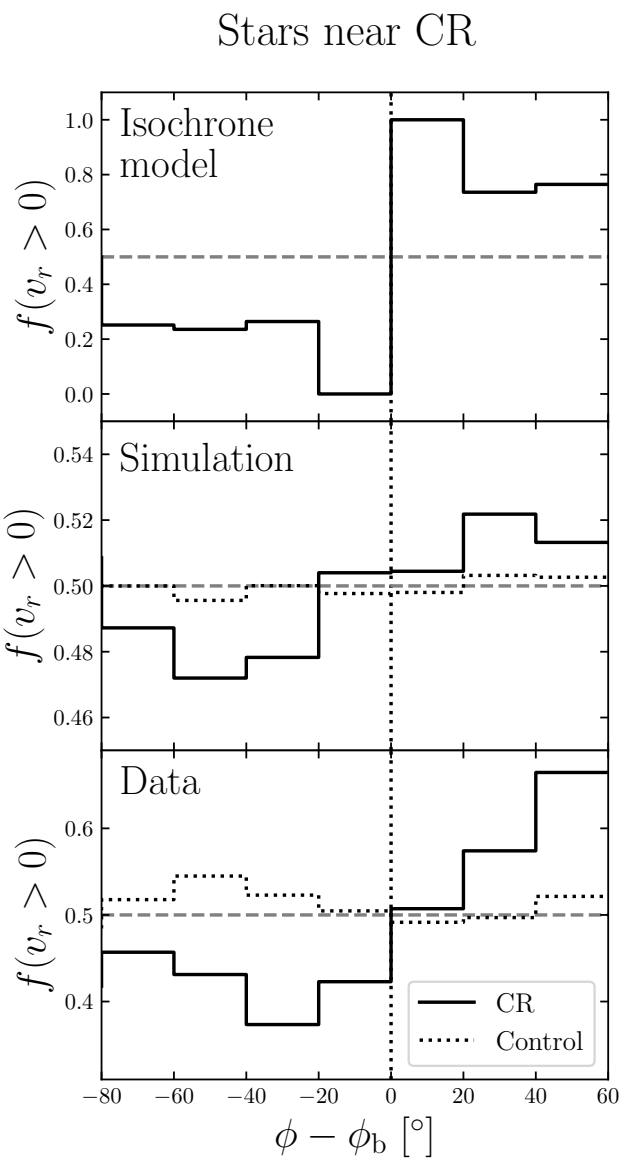

Figure 18. Fraction of stars near the corotation resonance with v_r as a function of azimuth. The dotted distributions in the lower two panels show control samples (i.e. stars not near CR). For the data a bar pattern speed of $\Omega_b = 35$ km s^{-1}kpc^{-1} is assumed. The vertical black dotted line marks the major axis of the bar, and the horizontal grey dashed line indicates an equal number of stars with positive and negative v_r.

is consistent with what is observed in data from *Gaia* DR3 for prograde stars, but not with chevrons arising from an ancient merger event (Donlon et al. 2023).

(iv) In action space (J_ϕ, J_r), the resonances lie along diagonal lines from high J_r at $J_\phi = 0$ to $J_r = 0$ at high $|J_\phi|$. Our analytic model and simulation predict that as J_ϕ is increased from zero, the mean v_r transitions from negative to positive along each of these bands. We find that such features are also visible in the data when the action space is colour-coded by mean v_r. At a bar pattern speed of $\Omega_b = 35$ km s^{-1} kpc^{-1} consistent with previous studies (e.g. Sanders et al. 2019; Chiba & Schönrich 2021; Clarke & Gerhard 2022), these features align reasonably well with the corotation (CR), outer Lindblad (OLR) and 1:1 resonances. The band we associate with the CR is continuous with the Hercules stream in the disc (at low J_r). This band extends as far as $J_\phi = 0$ and transitions to a mean $v_r < 0$ at $J_\phi \lesssim 800$.

(v) At $\Omega_b = 35$ km s^{-1}kpc^{-1}, we select stars from the data close to the predicted resonances. The distributions of these stars in radial phase space align almost exactly with the most prominent observed chevrons. In particular, the stars near CR closely match the innermost prograde chevron ('Chevron 1' in Belokurov et al. 2023) which peaks at $r \approx 10$ kpc. This chevron can therefore be seen as a highly eccentric counterpart of the Hercules stream. The next prograde chevron (Chevron 3) corresponds to the OLR. The clearest retrograde chevron (Chevron 2) does not match any of the predicted $m = 2$ resonances. However, it does reasonably match the $l/m = 5/4$ resonance. This may explain its lack of asymmetry.

(vi) We predict that the asymmetry in v_r should change as a function of position in the Galaxy. More resonant stars are expected to have v_r at larger radii ($r \gtrsim 13$ kpc) and on the opposite sides of the bar's major or minor axes. For stars near the CR, we find that this flip in asymmetry does appear to occur in the data on the opposite side of the bar's major axis. Future data samples may allow these predictions to be tested more comprehensively.

Our results show that the observed radial phase space of the Milky Way's halo closely matches many aspects of bar resonances in the models. Various features of the observed chevrons do not appear to be consistent with formation by an ancient merger event, such as the presence of the chevrons at high metallicity and the asymmetry in v_r (Belokurov et al. 2023). These observations are natural consequences of our dynamical explanation. We have shown that the prograde chevrons match the predicted locations of resonances, and can be directly related to moving groups in the disc widely associated with bar resonances. We conclude that there is a high probability that much of the substructure in (r, v_r) space results from trapping of halo stars by the bar. This means that the chevrons should not be used to infer the Milky Way's assembly history without extreme caution. However, it does offer possible avenues for future work to constrain properties of the Galactic bar, such as pattern speed and scale length.

ACKNOWLEDGEMENTS

We thank the Cambridge Streams group and attendees of the Galactic Bars 2023 conference for helpful comments and suggestions during this study. AMD thanks the Science and Technology Facilities Council (STFC) for a PhD studentship. VB and NWE acknowledge support from the Leverhulme Research Project Grant RPG-2021-205: "The Faint Universe Made Visible with Machine Learning".

This work has made use of data from the European Space Agency (ESA) mission *Gaia* (`https://www.cosmos.esa.int/gaia`), processed by the *Gaia* Data Processing and Analysis Consortium (DPAC, `https://www.cosmos.esa.int/web/gaia/dpac/consortium`). Funding for the DPAC has been provided by national institutions, in particular the institutions participating in the *Gaia* Multilateral Agreement.

This research made use of Astropy,[2] a community-developed core Python package for Astronomy (Astropy Collaboration et al. 2013,

[2] http://www.astropy.org

2018). This work was funded by UKRI grant 2604986. For the purpose of open access, the author has applied a Creative Commons Attribution (CC BY) licence to any Author Accepted Manuscript version arising.

DATA AVAILABILITY

This study uses publicly available *Gaia* data. Code used to calculate resonant orbits in the isochrone potential can be found at https://github.com/adllmr/isochrone_resonances.

REFERENCES

Amorisco N. C., 2017, MNRAS, 464, 2882
Antoja T., Figueras F., Fernández D., Torra J., 2008, A&A, 490, 135
Astropy Collaboration et al., 2013, A&A, 558, A33
Astropy Collaboration et al., 2018, AJ, 156, 123
Athanassoula E., 1992, MNRAS, 259, 345
Athanassoula E., 2002, ApJ, 569, L83
Bailer-Jones C. A. L., Rybizki J., Fouesneau M., Demleitner M., Andrae R., 2021, AJ, 161, 147
Belokurov V., Erkal D., Evans N. W., Koposov S. E., Deason A. J., 2018, MNRAS, 478, 611
Belokurov V., Vasiliev E., Deason A. J., Koposov S. E., Fattahi A., Dillamore A. M., Davies E. Y., Grand R. J. J., 2023, MNRAS, 518, 6200
Binney J., 2018, MNRAS, 474, 2706
Binney J., 2020, MNRAS, 495, 895
Binney J., Tremaine S., 2008, Galactic Dynamics: Second Edition
Bland-Hawthorn J., Gerhard O., 2016, ARA&A, 54, 529
Borderies N., Goldreich P., 1984, Celestial Mechanics, 32, 127
Ceverino D., Klypin A., 2007, MNRAS, 379, 1155
Chiba R., Schönrich R., 2021, MNRAS, 505, 2412
Chiba R., Schönrich R., 2022, MNRAS, 513, 768
Chiba R., Friske J. K. S., Schönrich R., 2021, MNRAS, 500, 4710
Chirikov B. V., 1979, Phys. Rep., 52, 263
Clarke J. P., Gerhard O., 2022, MNRAS, 512, 2171
Collett J. L., Dutta S. N., Evans N. W., 1997, MNRAS, 285, 49
Collier A., Shlosman I., Heller C., 2019, MNRAS, 488, 5788
Contopoulos G., 1979, A&A, 71, 221
D'Onghia E., L. A., J. A., 2020, ApJ, 890, 117
Davies E. Y., Dillamore A. M., Vasiliev E., Belokurov V., 2023a, arXiv e-prints, p. arXiv:2301.04154
Davies E. Y., Vasiliev E., Belokurov V., Evans N. W., Dillamore A. M., 2023b, MNRAS, 519, 530
Deason A. J., Belokurov V., Evans N. W., 2011, MNRAS, 416, 2903
Debattista V. P., Sellwood J. A., 1998, ApJ, 493, L5
Debattista V. P., Sellwood J. A., 2000, ApJ, 543, 704
Dehnen W., 2000, AJ, 119, 800
Dillamore A. M., Belokurov V., Evans N. W., Davies E. Y., 2023, MNRAS, 524, 3596
Dong-Páez C. A., Vasiliev E., Evans N. W., 2022, MNRAS, 510, 230
Donlon Thomas I., Newberg H. J., Sanderson R., Bregou E., Horta D., Arora A., Panithanpaisal N., 2023, arXiv e-prints, p. arXiv:2310.09376
Earn D. J. D., Lynden-Bell D., 1996, MNRAS, 278, 395
Eggen O. J., Lynden-Bell D., Sandage A. R., 1962, ApJ, 136, 748
Evans N. W., de Zeeuw P. T., Lynden-Bell D., 1990, MNRAS, 244, 111
Faccioli L., Smith M. C., Yuan H. B., Zhang H. H., Liu X. W., Zhao H. B., Yao J. S., 2014, ApJ, 788, 105
Feuillet D. K., Sahlholdt C. L., Feltzing S., Casagrande L., 2021, MNRAS, 508, 1489
Fillmore J. A., Goldreich P., 1984, ApJ, 281, 1
Fragkoudi F., et al., 2019, MNRAS, 488, 3324
Gaia Collaboration et al., 2016, A&A, 595, A1
Gaia Collaboration et al., 2023, A&A, 674, A1
Gerhard O., 2011, Memorie della Societa Astronomica Italiana Supplementi, 18, 185
Hamilton C., Tolman E. A., Arzamasskiy L., Duarte V. N., 2023, ApJ, 954, 12
Helmi A., Babusiaux C., Koppelman H. H., Massari D., Veljanoski J., Brown A. G. A., 2018, Nature, 563, 85
Henon M., 1959, Annales d'Astrophysique, 22, 126
Henrard J., 1982, Celestial Mechanics, 27, 3
Jeffreson S. M. R., et al., 2017, MNRAS, 469, 4740
Kalnajs A. J., 1977, ApJ, 212, 637
Kalnajs A. J., 1991, in Sundelius B., ed., Dynamics of Disc Galaxies. p. 323
Katz D., et al., 2023, A&A, 674, A5
Khoperskov S., Gerhard O., 2022, A&A, 663, A38
Khoperskov S., Gerhard O., Di Matteo P., Haywood M., Katz D., Khrapov S., Khoperskov A., Arnaboldi M., 2020, A&A, 634, L8
Lynden-Bell D., 1973, in Contopoulos G., Henon M., Lynden-Bell D., eds, Saas-Fee Advanced Course 3: Dynamical Structure and Evolution of Stellar Systems. p. 91
Lynden-Bell D., 1979, MNRAS, 187, 101
McMillan P. J., 2013, MNRAS, 430, 3276
McMillan P. J., 2017, MNRAS, 465, 76
Moreno E., Pichardo B., Schuster W. J., 2015, MNRAS, 451, 705
Moreno E., Fernández-Trincado J. G., Schuster W. J., Pérez-Villegas A., Chaves-Velasquez L., 2021, MNRAS, 506, 4687
Myeong G. C., Evans N. W., Belokurov V., Sanders J. L., Koposov S. E., 2018, ApJ, 856, L26
Naidu R. P., Conroy C., Bonaca A., Johnson B. D., Ting Y.-S., Caldwell N., Zaritsky D., Cargile P. A., 2020, ApJ, 901, 48
Pérez-Villegas A., Portail M., Wegg C., Gerhard O., 2017, ApJ, 840, L2
Pila-Díez B., de Jong J. T. A., Kuijken K., van der Burg R. F. J., Hoekstra H., 2015, A&A, 579, A38
Portail M., Gerhard O., Wegg C., Ness M., 2017, MNRAS, 465, 1621
Price-Whelan A. M., 2017, The Journal of Open Source Software, 2
Quinn P. J., 1984, ApJ, 279, 596
Sanders J. L., Smith L., Evans N. W., 2019, MNRAS, 488, 4552
Schönrich R., Binney J., Dehnen W., 2010, MNRAS, 403, 1829
Sellwood J. A., 2010, MNRAS, 409, 145
Sormani M. C., Magorrian J., Nogueras-Lara F., Neumayer N., Schönrich R., Klessen R. S., Mastrobuono-Battisti A., 2020, MNRAS, 499, 7
Sormani M. C., Gerhard O., Portail M., Vasiliev E., Clarke J., 2022, MNRAS, 514, L1
Tremaine S., Weinberg M. D., 1984, ApJ, 282, L5
Trick W. H., 2022, MNRAS, 509, 844
Trick W. H., Fragkoudi F., Hunt J. A. S., Mackereth J. T., White S. D. M., 2021, MNRAS, 500, 2645
Vasiliev E., 2019, MNRAS, 482, 1525
Watkins L. L., et al., 2009, MNRAS, 398, 1757
Wegg C., Gerhard O., Portail M., 2015, MNRAS, 450, 4050
Weinberg M. D., Katz N., 2002, ApJ, 580, 627
Wheeler A., Abril-Cabezas I., Trick W. H., Fragkoudi F., Ness M., 2022, ApJ, 935, 28
Yoder C. F., 1979, Celestial Mechanics, 19, 3
Zhang X., Green G. M., Rix H.-W., 2023, MNRAS, 524, 1855

APPENDIX A: ORBITS IN THE ISOCHRONE POTENTIAL

The angle variables θ_i in the isochrone potential can be expressed analytically in terms of the positions (r, θ, ϕ). We here present these transformations as given by Binney & Tremaine (2008). They are expressed in terms of the variable η, defined by

$$s = 2 + \frac{c}{b}(1 - e\cos\eta), \tag{A1}$$

where

$$c \equiv \frac{GM}{-2H_0} - b, \tag{A2}$$

$$e^2 \equiv 1 - \frac{L^2}{GMc}\left(1 + \frac{b}{c}\right), \tag{A3}$$

$$s \equiv 1 + \sqrt{1 + r^2/b^2}. \tag{A4}$$

The angles are then

$$\theta_r = \eta - \frac{ec}{c+b}\sin\eta, \tag{A5}$$

$$\theta_\theta = \psi + \frac{\Omega_\theta}{\Omega_r}\theta_r - \tan^{-1}\left(\sqrt{\frac{1+e}{1-e}}\tan\left(\tfrac{1}{2}\eta\right)\right) \tag{A6}$$

$$- \frac{1}{\sqrt{1+4GMb/L^2}}\tan^{-1}\left(\sqrt{\frac{1+e+2b/c}{1-e+2b/c}}\tan\left(\tfrac{1}{2}\eta\right)\right),$$

$$\theta_\phi = \Omega + \mathrm{sgn}(J_\phi)\theta_\theta. \tag{A7}$$

Here Ω is not a frequency, but instead is the longitude of the ascending node. This is the value of ϕ at which the particle crosses the $\theta = \pi/2$ plane with $\dot{\theta} < 0$ (i.e. $\dot{z} > 0$). ψ is the angle measured in the plane of the orbit from the ascending node to the current position of the particle. In the case of orbits confined to the $\theta = \pi/2$ plane, we may set $\Omega = 0$ and hence $\psi = \mathrm{sign}(J_\phi)\phi$ without loss of generality.

In practice we generate orbits by creating a grid in η, and calculate θ_r from this. By cubic interpolation we then find η as a function of a uniform grid in θ_r (i.e. equally spaced points in time along each orbit). All other quantities are then calculated.

APPENDIX B: CALCULATION OF G IN THE ISOCHRONE POTENTIAL

The pendulum equation 39 contains the quantity G, defined by equation 40. This can be written as (Chiba et al. 2021):

$$G = \frac{\partial}{\partial J_s}(m\Omega_\phi + l\Omega_r) \tag{B1}$$

$$= \left(m\frac{\partial}{\partial J_\phi} + l\frac{\partial}{\partial J_r}\right)(m\Omega_\phi + l\Omega_r) \tag{B2}$$

$$= m^2\frac{\partial\Omega_\phi}{\partial J_\phi} + ml\left(\frac{\partial\Omega_\phi}{\partial J_r} + \frac{\partial\Omega_r}{\partial J_\phi}\right) + l^2\frac{\partial\Omega_r}{\partial J_r}. \tag{B3}$$

We wish to analytically calculate G in the isochrone potential. As before we consider orbits confined to the $\theta = \pi/2$ plane, so that we may set $L = |J_\phi|$. It is convenient to define the parameter

$$\alpha \equiv \frac{1}{2}\left(1 + \frac{L}{\sqrt{L^2 + 4GMb}}\right). \tag{B4}$$

The derivatives of the frequencies (equations 10 and 12) with respect to the actions can then be written as

$$\frac{\partial\Omega_r}{\partial J_r} = -3\Omega_r\left[J_r + \frac{\alpha}{2\alpha - 1}L\right]^{-1}, \tag{B5}$$

$$\frac{\partial\Omega_r}{\partial J_\phi} = \frac{\partial\Omega_\phi}{\partial J_r} = \alpha\,\mathrm{sgn}(J_\phi)\frac{\partial\Omega_r}{\partial J_r}, \tag{B6}$$

$$\frac{\partial\Omega_\phi}{\partial J_\phi} = \alpha^2\frac{\partial\Omega_r}{\partial J_r} + \frac{\partial\alpha}{\partial J_\phi}\mathrm{sgn}(J_\phi)\Omega_r \tag{B7}$$

$$= \alpha^2\frac{\partial\Omega_r}{\partial J_r} + 2\alpha(1-\alpha)(2\alpha-1)\frac{\Omega_r}{L}. \tag{B8}$$

Therefore G can be expressed as

$$G = \left[l + m\alpha\,\mathrm{sgn}(J_\phi)\right]^2\frac{\partial\Omega_r}{\partial J_r} + 2m^2\alpha(1-\alpha)(2\alpha-1)\frac{\Omega_r}{L}. \tag{B9}$$

We can evaluate this expression as a function of J_ϕ along the resonances using equations 10, 16 and B5. An equivalent expression is given in Earn & Lynden-Bell (1996).

APPENDIX C: TEST PARTICLE SIMULATION SETUP

In our simulations the relative strength of the non-axisymmetric multipole components representing the bar evolves according to

$$\beta(t) = \begin{cases} \frac{3}{16}\xi^5 - \frac{5}{8}\xi^3 + \frac{15}{16}\xi + \frac{1}{2} & t < t_1 \\ 1 & t \geq t_1, \end{cases} \tag{C1}$$

$$\xi \equiv 2\frac{t}{t_1} - 1. \tag{C2}$$

This form matches that used by Dehnen (2000). The bar's pattern speed evolves according to

$$\Omega_b(t) = \begin{cases} \Omega_i & t < t_1 \\ \Omega_i\left[1 + \frac{1}{2}\eta\,\Omega_i(t-t_1)^2/(t_2-t_1)\right]^{-1} & t_1 \leq t < t_2 \\ \Omega_2\left[1 + \eta\,\Omega_2(t-t_2)\right]^{-1} & t \geq t_2, \end{cases} \tag{C3}$$

$$\Omega_2 \equiv \Omega_i\left[1 + \frac{1}{2}\eta\,\Omega_i(t_2 - t_1)\right]^{-1}, \tag{C4}$$

where $\eta \equiv -\dot{\Omega}_b/\Omega_b^2$. We choose $t_1 = 2$ s kpc/km ≈ 2 Gyr and $t_2 \approx 3$ Gyr. We set the initial pattern speed to $\Omega_i = 80\,\mathrm{km\,s^{-1}kpc^{-1}}$ and the deceleration parameter to $\eta = 0.003$.

This paper has been typeset from a TEX/LATEX file prepared by the author.